Comparison of Urban Air Quality Simulations During the KORUS-AQ Campaign With Regionally Refined Versus Global Uniform Grids in the Multi-Scale Infrastructure for Chemistry and Aerosols (MUSICA) Version 0

Duseong S. Jo[1,2] , Louisa K. Emmons[1] , Patrick Callaghan[3], Simone Tilmes[1] , Jung-Hun Woo[4] , Younha Kim[5], Jinseok Kim[4], Claire Granier[6,7] , Antonin Soulié[6], Thierno Doumbia[6] , Sabine Darras[8], Rebecca R. Buchholz[1] , Isobel J. Simpson[9] , Donald R. Blake[9] , Armin Wisthaler[10,11] , Jason R. Schroeder[12,13], Alan Fried[14] , and Yugo Kanaya[15]

[1]Atmospheric Chemistry Observations and Modeling Laboratory, National Center for Atmospheric Research, Boulder, CO, USA, [2]Advanced Study Program, National Center for Atmospheric Research, Boulder, CO, USA, [3]Climate and Global Dynamics Laboratory, National Center for Atmospheric Research, Boulder, CO, USA, [4]Konkuk University, Seoul, South Korea, [5]International Institute for Applied Systems Analysis, Laxenburg, Austria, [6]Laboratoire d'Aérologie, CNRS, Université de Toulouse, Toulouse, France, [7]NOAA/Chemical Sciences Laboratory, CIRES, University of Colorado, Boulder, CO, USA, [8]Observatoire Midi-Pyrénées, Toulouse, France, [9]University of California, Irvine, CA, USA, [10]Department of Chemistry, University of Oslo, Oslo, Norway, [11]Institute for Ion Physics and Applied Physics, University of Innsbruck, Innsbruck, Austria, [12]NASA Langley Research Center, Hampton, VA, USA, [13]Now at California Air Resources Board, Sacramento, CA, USA, [14]Institute of Arctic and Alpine Research, University of Colorado, Boulder, CO, USA, [15]Japan Agency for Marine-Earth Science and Technology, Yokohama, Japan

Abstract Model intercomparison studies often report a large spread in simulation results, but quantifying the causes of these differences is hindered by the fact that several processes contribute to the model spread simultaneously. Here we use the Multi-Scale Infrastructure for Chemistry and Aerosols (MUSICA) version 0 to investigate the model resolution dependencies of simulated chemical species, with a focus on the differences between global uniform grid and regional refinement grid simulations with the same modeling framework. We construct two global (ne30 [~112 km] and ne60 [~56 km]) and two regional refinement grids over Korea (ne30x8 [~14 km] and ne30x16 [~7 km]). The grid resolution can change chemical concentrations by an order of magnitude in the boundary layer, and the importance increases as the species' reactivity increases (e.g., up to 50% and 1,000% changes for ethane and xylenes, respectively). The diurnal cycle of oxidants (OH, O_3, and NO_3) also varies with the grid resolution, which leads to different oxidation pathways of volatile organic compounds (e.g., the fraction of monoterpenes reacting with NO_3 in Seoul around midnight is 90% for ne30, but 65% for ne30x16). The models with high-resolution grids usually do a better job at reproducing aircraft observations during the KORUS-AQ campaign, but not always, implying compensating errors in the coarse grid simulations. For example, ozone is better reproduced by the coarse grid due to the artificial mixing of NO_x. When developing new chemical mechanisms and evaluating models over urban areas, the uncertainties associated with model resolution should be considered.

Plain Language Summary A new model framework, the Multi-Scale Infrastructure for Chemistry and Aerosols version 0 (MUSICAv0), has been developed at NCAR to enable a computationally feasible global modeling framework while still resolving chemistry at urban scales. Using the MUSICAv0 framework with different horizontal grid resolutions (~112, ~56, ~14, and ~7 km), this work examines how much horizontal grid resolution can affect simulated chemical concentrations in 3D chemistry models. Model concentrations can vary up to 10 times between ~112 and ~7 km grids over urban areas at the surface. On the other hand, a region-specific emission inventory with detailed local information is essential for some chemical species, although it is generally less important than the grid resolution for many chemical species. The model with a high-resolution grid better reproduces observations in general, but in some cases compensating errors result in better comparisons for the coarse grid. This work suggests that the effects of grid resolution should not be ignored when evaluating new chemical mechanisms and chemistry models in future studies, and high grid resolution in 3D models is needed to simulate air pollutants over urban and downwind regions.

1. Introduction

Chemistry models play a vital role in understanding atmospheric processes of gases and aerosols and their effects on radiation, visibility, and health. Chemistry models help to shed light on the complex interplay of chemistry, emission, transport, and deposition (Brasseur & Jacob, 2017). Additionally, global implications of new chemical species and chemistry can be estimated using 3D global chemistry models (e.g., Jo et al., 2021; Paulot et al., 2009; Veres et al., 2020). Accurate representation of each atmospheric process is crucial for these applications, as biases in surface concentrations can lead to incorrect estimates of deaths attributable to air pollution (Paolella et al., 2018; Punger & West, 2013).

There are several ways to improve the model performance, and much effort has been made to improve physical and chemical processes in the model, such as the chemical mechanism and deposition processes (Clifton et al., 2020; Schwantes et al., 2020). However, relatively less attention has been given to the model framework and associated intrinsic characteristics, which can be as important as the chemical mechanism. Even with the same dynamical core, physics package, chemical mechanism, and initial/boundary conditions, model results can vary due to simulation parameters such as horizontal resolution and timestep (Pfister et al., 2020).

Global chemistry models are often used to investigate the global and regional distribution of air pollutants (Fairlie et al., 2020; Schwantes et al., 2020), as they can deliver significant implications to research findings on a global scale (H. Brown et al., 2018; Jo et al., 2016). Horizontal resolutions of global models are typically 0.5°~5° with recent trends toward finer resolutions as shown in AeroCom model intercomparison studies (Bian et al., 2017; Gliß et al., 2021; Tsigaridis et al., 2014). While these coarse grids may be sufficient for reproducing air pollutants in rural/remote areas, they can fail to simulate air pollutants in urban areas (Jo et al., 2013). Recent studies have developed global chemistry models with 12.5–14 km grid spacing but are computationally very expensive (Goto et al., 2020; Hu et al., 2018). To address this issue, stretched grids or nested versions of global chemistry models have been developed since the mid-2000s (Krol et al., 2005; Park et al., 2004; Y. X. Wang et al., 2004). Recent nested grid resolutions ($0.25° \times 0.3125°$; Kim et al., 2015) have become comparable to those of regional models, as used in a continent-scale model intercomparison study (15~60 km) (Gao et al., 2018), but the resolutions are still coarser than a country-scale model intercomparison study (4~27 km) (Park et al., 2021). Stretched grids are also actively being developed. For example, GEOS-Chem has recently developed a cubed-sphere grid version called GEOS-Chem High Performance (GCHP) (Eastham et al., 2018), which has been used for stretched-grid simulations over the US (C180; ~57 km) and California (C900; ~11 km) (Bindle et al., 2021).

Several studies have investigated the effects of grid resolution on chemistry simulation. Zakoura and Pandis (2018) showed that even a 36 km resolution simulated different nitrate concentrations (~a factor of 2) compared to 12 and 4 km resolutions, due to the artificial mixing of NO_x-rich plumes, causing different nighttime nitrate production rates. Yu et al. (2016) reported that formaldehyde was overestimated at coarse global resolutions ($2.0° \times 2.5°$ and $4.0° \times 5.0°$) but NO_x (sum of NO and NO_2), ozone, and isoprene concentrations showed little difference across model resolutions ($0.25° \times 0.3125°$, $2.0° \times 2.5°$, and $4.0° \times 5.0°$) over the Southeast US. A study by Schaap et al. (2015), which used five regional chemical transport models, showed that increasing the model resolution from ~50 to ~14 km is beneficial for European-scale applications. Although the model grid resolutions used in these studies were still not sufficient to resolve urban or biomass burning plumes, which require a spatial resolution of 1 km or less (Meidan et al., 2019; S. Wang et al., 2021), high-resolution grids generally showed better agreements with observations.

Most previous studies have been limited to investigations of only a few species (e.g., NO_x, ozone, particulate matter). However, the results can vary depending on the species with different sources and reactivities. A more thorough understanding of how different resolutions affect chemistry simulations is needed as chemistry models progress to higher resolutions with new techniques such as regional refinement in widely used global chemistry models (e.g., CAM-chem and GEOS-Chem; Bindle et al., 2021; Schwantes et al., 2022). Additionally, changes in dynamics fields caused by different spatial and temporal resolutions can also have an impact on chemistry simulations for models that calculate dynamics online (e.g., CAM-chem), as opposed to chemical transport models that are driven by meteorological input (e.g., GEOS-Chem).

Here we use the Community Earth System Model/Community Atmosphere Model with full chemistry (CESM/CAM-chem) using the Spectral Element (SE) with Regional Refinement (RR) dynamical core (Schwantes et al., 2022) to examine the effects of grid resolution on a variety of chemical species. CESM/CAM-chem-SE-RR

is also the initial version of the Multi-Scale Infrastructure for Chemistry and Aerosols (MUSICA) and is called MUSICAv0 (Pfister et al., 2020). MUSICAv0 has many advantages over traditional global and regional models, in that global and regional scales are simulated within one model with consistent chemistry and dynamics. Since regional models require lateral boundary conditions from a global model, inconsistencies can be introduced due to different chemical mechanisms used in the global and regional models. Furthermore, consistent simulations of long-lived species inside and outside of the regional domain by MUSICAv0 allow consistent background levels of oxidants and long-range transport processes. Tang et al. (2023) demonstrated that MUSICAv0 with regional refinement provides improved simulation of long-range transport of fire plumes and stratospheric intrusions compared to regional models. Two-way feedback from local to global scales, in terms of land and atmosphere interactions as well as meteorology and chemistry, can also be better captured by the unified framework in MUSICAv0.

This study is one of the first custom grid applications of MUSICAv0, where we compare two global grids (ne30 [~112 km] and ne60 [~56 km]) and two regional refinement grids over Korea (ne30x8 [~14 km] and ne30x16 [~7 km]). Tools to create custom grids and associated meteorological, chemical, and emission input files are made available to the modeling community (https://wiki.ucar.edu/display/MUSICA/MUSICA+Home). We perform chemistry simulations for the Korea-United States Air Quality (KORUS-AQ) campaign when extensive field measurements are available over urban regions (Crawford et al., 2021).

The spatial resolution of emission inventories has also been improved to keep pace with the model framework development. Even global emission inventories have a horizontal resolution of 0.1° (Crippa et al., 2018; Elguindi et al., 2020), which is comparable to the horizontal resolution of regional inventories (Kurokawa & Ohara, 2020; Marais & Wiedinmyer, 2016). On the other hand, in order to accurately simulate chemical concentrations, up-to-date information is essential especially for chemical species regulated by air quality policies. Regional emission inventories are more advantageous as they often use local information written in the local language and can be updated more quickly than global inventories. During the KORUS-AQ campaign, a regional emission inventory was specially developed with up-to-date local statistics and policy (KORUSv5; Section 2.3). Comparing model results simulated by different grid resolutions using different up-to-date global and regional emission inventories can provide guidance for future studies, as regional refinement models are expected to be increasingly used as a next-generation chemistry model (Pfister et al., 2020).

In this work, we present a systematic study of model resolution dependencies of simulated chemical species for various aspects, with a focus on the differences between global uniform grid simulations and regional refinement grid simulations. In the following sections, ozone, CO, NO_x, NO_y (sum of NO_x, PAN, HNO_3, N_2O_5, HO_2NO_2, and other reactive nitrogen compounds), alkanes, aromatics, biogenic emissions, and OH reactivities are discussed in terms of model representativeness of urban and rural areas. The changes in simulation results due to the emission inventory used are also investigated, together with the diurnal cycle and NO_x speciation of anthropogenic emissions with different horizontal resolutions. Finally, model results are evaluated against aircraft and surface observations over different chemical regimes during KORUS-AQ.

2. Model Description

2.1. General

MUSICAv0 (available in CESM2.2) has been used to conduct a global three-dimensional simulation of chemistry with regional refinement over East Asia and the Korean peninsula (Section 2.2). The SE dynamical core is used to allow unstructured grid simulations with variable resolution (Lauritzen et al., 2018). The planetary boundary layer (PBL), shallow convection, and macrophysics are simulated using the Cloud Layers Unified by Binormals (Bogenschutz et al., 2013; Golaz et al., 2002). The deep convection is parameterized using the Zhang and McFarlane (1995) (ZM) scheme. The cloud microphysics is simulated using the MG2 scheme (Gettelman & Morrison, 2015), which is coupled with the four-mode version of the Modal Aerosol Module (Liu et al., 2016). The radiation scheme is the Rapid Radiative Transfer Model for General Circulation Models (Iacono et al., 2008). The Community Land Model version 5 (CLM5) is coupled online for calculating land model processes (Lawrence et al., 2019).

Simulations are conducted for the KORUS-AQ campaign in May–June 2016 (Crawford et al., 2021), with two spin-up processes. First, a CESM simulation is performed for 5 years without detailed chemistry (i.e., CAM) to
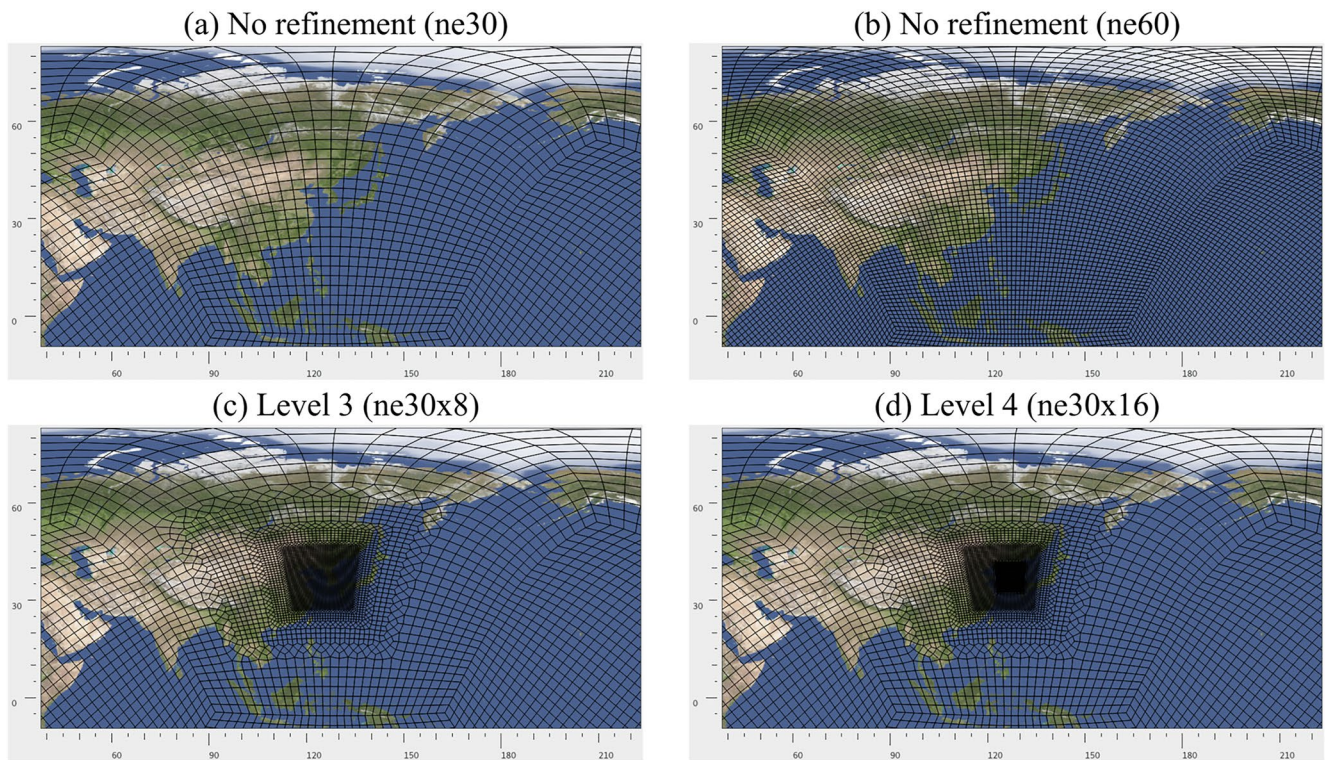
Figure 1. The variable-resolution grid element map of Community Earth System Model Spectral Element dynamical core. (a) Global ne30 grid, (b) global ne60 grid, (c) regional refinement ne30x8 grid, and (d) regional refinement ne30x16 grid.

generate initial conditions for CLM5. Second, to generate initial conditions for chemical tracers, CESM with the MOZART-TS1 chemical mechanism (i.e., CAM-chem) is run for 16 months on each grid. To ensure enough spin-up period for long-lived species, the CAM-chem simulation starts from a fully spun-up CAM-chem restart file on a finite volume grid (Emmons et al., 2020) which is regridded to the SE grids for this study.

For the simulations analyzed in this study, temperature and horizontal winds are nudged toward the Modern-Era Retrospective analysis for Research and Applications version 2 (MERRA2) (Gelaro et al., 2017). The MERRA2 meteorological fields are available at $0.625° \times 0.5°$ resolution every 3 hr but are regridded to four SE grids for this study. Nudging is not applied within the regionally refined region (ne30x8 and ne30x16), where the resolution of the original MERRA2 is coarser than the model grid, in order to avoid the influences of coarse meteorological fields on the much higher spatial resolution calculation. In all model plots and analyses, the chemical concentration at the surface is the value in the lowest model layer.

2.2. Grid Setup

The four SE grids used in this study were generated using the Community Mesh Generation Toolkit (https://github.com/ESMCI/Community_Mesh_Generation_Toolkit) which provides programs to create rotated and regionally refined grids for a desired resolution. To avoid edges and corners near the region of interest, the cubed sphere was rotated to approximately center the KORUS-AQ domain on a cube face. As shown in Figure 1 (panels a and b), the spectral elements for the uniform (ne30) and (ne60) grids are created by subdividing each cube face into (30x30) and (60x60) elements, respectively. The "ne" resolution label stands for the number of elements in each coordinate direction on a cube face (Lauritzen et al., 2018).

For the two refined grids (panels c and d), the elements of the ne30 grid over the Korean peninsula are further subdivided into ne30x8 and ne30x16 resolutions, with the refined regions for these corresponding to elements with ne240 (~1/8th degree) and ne480 (~1/16th degree) resolutions, respectively. A halo region is added to separate each resolution transition. This is to minimize possible errors that may result from sharp resolution changes over short distances. The final computational grids used in the simulations are obtained by adding 4×4

Table 1
Total Emissions for May and June 2016 in the KORUSv5 and CAMS-GLOB-ANTv5.1 Anthropogenic Emission Inventories

Species	KORUSv5 (Gg)		CAMSv5.1 (Gg)		Difference (%)	
	East China	South Korea	East China	South Korea	East China	South Korea
CO	6,852	266	6,456	599	6	−56
NO_x	904	155	983	172	−8	−10
NO	772	129	983	172	−21	−25
NO_2	132	27	N/A	N/A	N/A	N/A
SO_2	521	53	1,632	126	−68	−58
C_2H_6	96	5.0	17	2.0	467	153
C_3H_8	85	6.5	67	12	27	−45
NH_3	435	49	343	55	27	−12
BIGALK[a]	442	33	337	38	31	−15
BIGENE[b]	89	7.6	49	4.9	83	54
BENZENE	23	2.9	50	4.3	−54	−33
TOLUENE	359	45	104	6.7	245	576
XYLENES	150	24	182	14	−18	68

Note. The relative differences between the KORUSv5 and CAMSv5.1 are shown in the two right columns. East China and South Korea domains are defined as (27.7°–40°N, 115–123°E) and (34.5°–38°N, 126–130°E), respectively.

[a]Lumped alkanes C ≥ 4. [b]Lumped alkenes C ≥ 4.

Gaussian-Legendre-Lobatto (GLL) grid points to each element to support third-order Legendre basis functions (Lauritzen et al., 2010), resulting in irregular grid spacing (Figure S1 in Supporting Information S1). The resulting high-resolution regions over Korea have grid spacings of approximately 14 and 7 km.

The model dynamical core, physics package, and chemical mechanism are the same for each of these grids, although the simulated meteorological and chemical fields may differ due to different horizontal grids and computational time steps. The offline emissions are mapped to the four different grids using the first-order conservative method (Jones, 1999) (Section 2.3). This method is also used to regrid the model output, allowing for direct comparison of different resolutions in the analysis section. The physics and dynamics time steps required for stable simulations decrease as the resolution increases. For the physics time step, 1,800, 900, 225, and 225 s are used for ne30, ne60, ne30x8, and ne30x16, respectively. Dynamics time steps of 300, 150, 37.5, and 18.75 s are chosen for ne30, ne60, ne30x8, and ne30x16 resolutions, following the recommendations of Herrington and Reed (2020).

2.3. Emissions

Two anthropogenic emission inventories are used in this work. The Copernicus Atmospheric Monitoring System version 5.1 (CAMS-GLOB-ANTv5.1) is used (Elguindi et al., 2020) for global emissions outside of Asia. Within the Asia region, either the CAMS-GLOB-ANTv5.1 or the KORUSv5 inventory is used to investigate the effects of emissions on air quality simulation with different grid resolutions.

The CAMS-GLOB-ANTv5.1 inventory is based on two global emission inventories. The Emissions Database for Global Atmospheric Research (EDGAR) v5 (Crippa et al., 2019) is used up to 2015, while the recent Community Emissions Data System (CEDS) (McDuffie et al., 2020) is used to extrapolate the emissions from 2016 to 2021. The speciation of Non-Methane Volatile Organic Compounds (NMVOC) is based on Huang et al. (2017), which is available until 2012. The same speciation is utilized for the time period from 2013 onwards with time-varying total NMVOC emissions.

The KORUSv5 emission inventory was developed in support of the KORUS-AQ field campaign, which took place in May–June 2016 (Park et al., 2021). There were several updates between v1 and v5 based on the findings during the field campaign, such as increased aromatic emissions in v5 compared to v1 (Park et al., 2021). The findings from the Megacity Air Pollution Studies-Seoul (MAPS-Seoul) campaign in 2015 were also used to develop the KORUSv5 inventory. In addition to the official statistics reported to international organizations, other detailed local statistics were also collected and incorporated into the emissions, with political factors such as control efficiency, rule penetration, and rule effectiveness in South Korea.

The total emissions of key anthropogenic species in the model are shown in Table 1. There are notable differences between the KORUSv5 and CAMS-GLOB-ANTv5.1 inventories even for major pollutants: the CO emissions in KORUSv5 are approximately half of those in CAMS-GLOB-ANTv5.1, and CAMS-GLOB-ANTv5.1 inventory has three times as much SO_2 as KORUSv5. The largest difference is seen for toluene, which is seven times higher in KORUSv5 for South Korea. The VOC speciation in the KORUSv5 inventory was specially developed for South Korea in 2016, whereas the VOC speciation in the CAMS-GLOB-ANTv5.1 inventory is the same for all Asian countries based on 2012 data (Huang et al., 2017). The SO_2 emissions were also significantly updated in KORUSv5 especially for large point sources. The KORUSv5 inventory speciates NO_x into NO and NO_2, while CAMS-GLOB-ANTv5.1 assumes NO_x as NO. Both inventories are available at 0.1° × 0.1° spatial resolution and are regridded to four different grids in this study. Sulfate emissions from the industrial and energy sectors are distributed up to 400 m to account for plume rise and stack height.

The aircraft emissions are from the CAMS-GLOB-AIR aviation emission inventory v2.1, which is available at 0.5° × 0.5° spatial resolution (Granier et al., 2019). This inventory is based on a combination of the CEDS

(Hoesly et al., 2018) and the EDGAR v4.3.1 data (Crippa et al., 2018) and is linearly extrapolated until 2020. The aircraft emissions of NO_2, SO_2, and black carbon (BC) are considered. Two types of volcanic SO_2 emissions are also included: continuously outgassing volcanoes (Diehl et al., 2012) and explosive volcanic eruptions from the Volcanic Emissions for Earth System Models v3.12 database (Mills et al., 2016; Neely & Schmidt, 2016).

The biomass burning emissions are calculated using two estimates, the Quick Fire Emissions Dataset (QFED) v2.5_r1 (Darmenov and da Silva, 2015) and the Fire INventory from NCAR (FINN) v1.5 (Wiedinmyer et al., 2011). Global CO_2 emissions from QFED v2.5_r1 are multiplied by emission factors collated for FINN v1.5 to construct the emission of each chemical species required in MUSICAv0 simulations.

The biogenic emissions are calculated online using the Model of Emissions of Gases and Aerosols from Nature (MEGAN) v2.1 (Guenther et al., 2012). Unlike the offline emissions, the emission totals vary depending on the land model (CLM5) configurations and spatial resolutions used. Several factors, such as temperature, solar radiative flux, and leaf area index (LAI) affect the online biogenic emissions. CLM5 provides two options to estimate LAI: one based on prescribed satellite phenology (SP option, with LAI at 0.25° resolution) and one using the prognostic vegetation state and active biogeochemistry (BGC option, which is resolved at the model grid) (Lawrence et al., 2019). Resolving topography at finer resolutions can provide detailed local surface temperature and solar radiation, and thus the resulting biogenic emissions. The changes in biogenic emissions due to different horizontal resolutions and CLM5 configurations are discussed in Section 3.3.

The calculation of lightning NO_x is also performed online within the model, based on the parameterization by Price et al. (1997). The production of lightning NO_x is dependent on the horizontal resolution (Tost et al., 2007). To account for this, the lightning NO_x production for the ne60, ne30x8, and ne30x16 grids is rescaled to match that of the ne30 grid simulation. The production of lightning NO_x over the study region (32°–38°N, 122–130°E) is small (0.05%) but it can still affect the background concentration of long-lived species.

The ocean and soil emissions are obtained from the Precursors of Ozone and their Effects in the Troposphere (POET) inventory (Granier et al., 2005) with the exception of dimethyl sulfide, which is obtained from the CAMS-GLOB-OCE v3.1 inventory (Granier et al., 2019).

2.3.1. Diurnal Cycle

In this study, we incorporate the diurnal variation into the monthly CAMS-GLOB-ANTv5.1 and KORUSv5 emissions and evaluate the impact of this variation on air quality simulations. It is worth noting that the current default CAM-chem and MUSICAv0 do not account for diurnal variations in anthropogenic emissions, and the KORUSv5 inventory was only available as monthly means in previous studies. In this study, we have updated CAM-chem and MUSICAv0 to consider the diurnal cycle of emissions in the model, based on the local time used in each country to reflect human activity patterns. The diurnal factors for the KORUSv5 inventory are newly derived as discussed below.

For the CAMS-GLOB-ANTv5.1 emissions, we use country and sector-specific hourly profiles reported by Crippa et al. (2020). These profiles were initially developed for the EDGAR inventory but are used here for the CAMS-GLOB-ANTv5.1 inventory, which is based on the EDGAR inventory (Section 2.3). The hourly diurnal profiles of the EDGAR sectors are illustrated in Figure S2a in Supporting Information S1.

For the KORUSv5 inventory, the diurnal emission factors are generated based on the SMOKE-Asia framework that provides sector-specific temporal profiles (Woo et al., 2012). The area source includes industry, solvent use, and residential subsectors, while the mobile source includes on-road and non-road subsectors. The point sources include industry and power generation subsectors. The sector-specific profiles in SMOKE-Asia framework are regionalized to accurately reflect the temporal variations of Asian activities based on default values in SMOKE for the United States. The diurnal emissions are calculated by detailed sector and then aggregated for the area and point sources, as well as the mobile sources (Figure S2b in Supporting Information S1).

2.4. Observations

The observations by the NASA DC-8 research aircraft during the KORUS-AQ campaign are used in this study (Section 4.1) to evaluate the model results. The DC-8 flew 20 sorties during the daytime (8–16 KST) from 2 May to 10 June 2016. All measurements used for this study have been described in previous studies (Crawford

Table 2
List of Simulations to Assess the Effects of Grid Resolution, Emission, and Other Model Configurations on Air Quality Simulation in South Korea

Simulation label	Asian inventory	Temporal resolution	NO$_x$ speciation	Details	Grid resolution
KORUS_D	KORUSv5	Monthly + Diurnal	Specified[a]		ne30, ne60, ne30x8, ne30x16
KORUS_DT				Same as KORUS_D but the time step for ne30x16 resolution is used	ne30
KORUS_BGC				Same as KORUS_D but BGC option is used for estimating LAI	ne30, ne30x16
KORUS_DN			All as NO		
KORUS_M		Monthly	Specified[a]		
CAMS_D	CAMSv5.1	Monthly + Diurnal	All as NO		
CAMS_M		Monthly			

Note. The global emissions inventory is the same for all simulations (CAMS-GLOB-ANTv5.1) listed here.

[a]See Table 1 for the NO:NO$_2$ ratio in the KORUS v5 inventory.

et al., 2021; Schroeder et al., 2020), but the measurements relevant to this study are briefly described below.

Ozone, NO, NO$_2$, and NO$_y$ were measured using the NCAR 4-channel chemiluminescence instrument with an uncertainty of 10% for ozone, 20% for NO, and 30% for NO$_2$ and NO$_y$ (Weinheimer et al., 1994). CO was measured by the Differential Absorption CO Measurement (DACOM) with an uncertainty of 2% (Sachse et al., 1991). HNO$_3$ was measured by the California Institute of Technology Chemical Ionization Mass Spectrometer with an uncertainty of 30% and a detection limit of 50 pptv (Crounse et al., 2006; Fahey et al., 2001). PAN and SO$_2$ were measured using the Georgia Tech CIMS with uncertainties of 30% and 20%, and detection limits of 2 and 20 pptv, respectively (Slusher et al., 2004). Benzene, toluene, ethane, isoprene, and cyclopentane were measured through whole air sampling (WAS) followed by multi-column gas chromatography (Simpson et al., 2020). The accuracy and detection limits for those VOCs were <5% and 3 pptv, respectively. Isoprene was additionally measured by a Photon Transfer Reaction Mass Spectrometer (PTR-MS) (Müller et al., 2014) with an accuracy of 10%. The measurements of isoprene by the two different instruments showed significant differences, as described in detail in Section 4.1. Acetaldehyde was also measured using the PTR-MS with an uncertainty of 25%. Formaldehyde was measured using the Compact Atmospheric Multi-species Spectrometer (CAMS, not to be confused with the model with the same acronym) with an average uncertainty of 5% (Richter et al., 2015). An Airborne Tropospheric Hydrogen Oxides Sensor (Brune et al., 2022) was used to measure OH and HO$_2$ with an uncertainty of 32%.

We also utilized surface measurements of ozone and CO at four locations with different chemical regimes (Section 4.2). At Olympic Park (urban), Ecotech gas sensors were used to measure ozone (EC9810) and CO (EC9830). At Taehwa Research Forest (urban downwind), ozone and CO were measured by Thermo Scientific 49i and 48i instruments, respectively. At Baengnyeong Island (rural), Teledyne gas analyzers were used to measure ozone and CO. Finally, Fukue Island was chosen as representative of remote/pristine regions, and ozone and CO were measured there using Thermo analyzers (49 and 48C) with 5% uncertainty for ozone and 20% for CO.

3. Differences in Model Results Between Regional Refinement and Global Grid Runs

Seven simulations are presented in this study, each with different grids and emissions: two simulations using the CAMS-GLOB-ANTv5.1 inventory (CAMS_D and CAMS_M), five simulations using the KORUS v5 inventory (KORUS_M, KORUS_D, KORUS_DN, KORUS_DT, and KORUS_BGC). A summary of these simulations can be found in Table 2. The CAMS_D simulation includes the diurnal cycle of emission flux, while the CAMS_M simulation does not. The KORUS_M simulation also does not include the diurnal cycle of emission flux, while the KORUS_D and KORUS_DN simulations both include the diurnal cycle with different NO$_x$ speciation. The KORUS_DT simulation is a ne30 simulation with a ne30x16 timestep to isolate the effects of timestep change. The KORUS_BGC simulation uses the interactive BGC option for the land model (CLM5) instead of the SP option (satellite LAI) to investigate the effects of regional refinement on vegetation state and biogenic emissions.

3.1. Effects of Regional Refinement on the Meteorological Fields

In this section, we examine the effects of regional refinement on the simulated meteorological fields, in terms of horizontal resolution and timestep. We compare the results from four different horizontal resolutions (KORUS_D; KORUSv5 emission with the diurnal emission cycle) The ne30 grid run from the KORUS_DT (ne30x16 timestep is used for the ne30 grid) is also compared. To ensure stability, we compare only the ne30 resolution runs with ne30 and ne30x16 timesteps as high-resolution grids are not suitable for longer timesteps.

Figure 2 shows the time series of meteorological fields averaged over the study region (32°–40°N, 122–130°E). The simulated fields are generally consistent, with small biases between the different
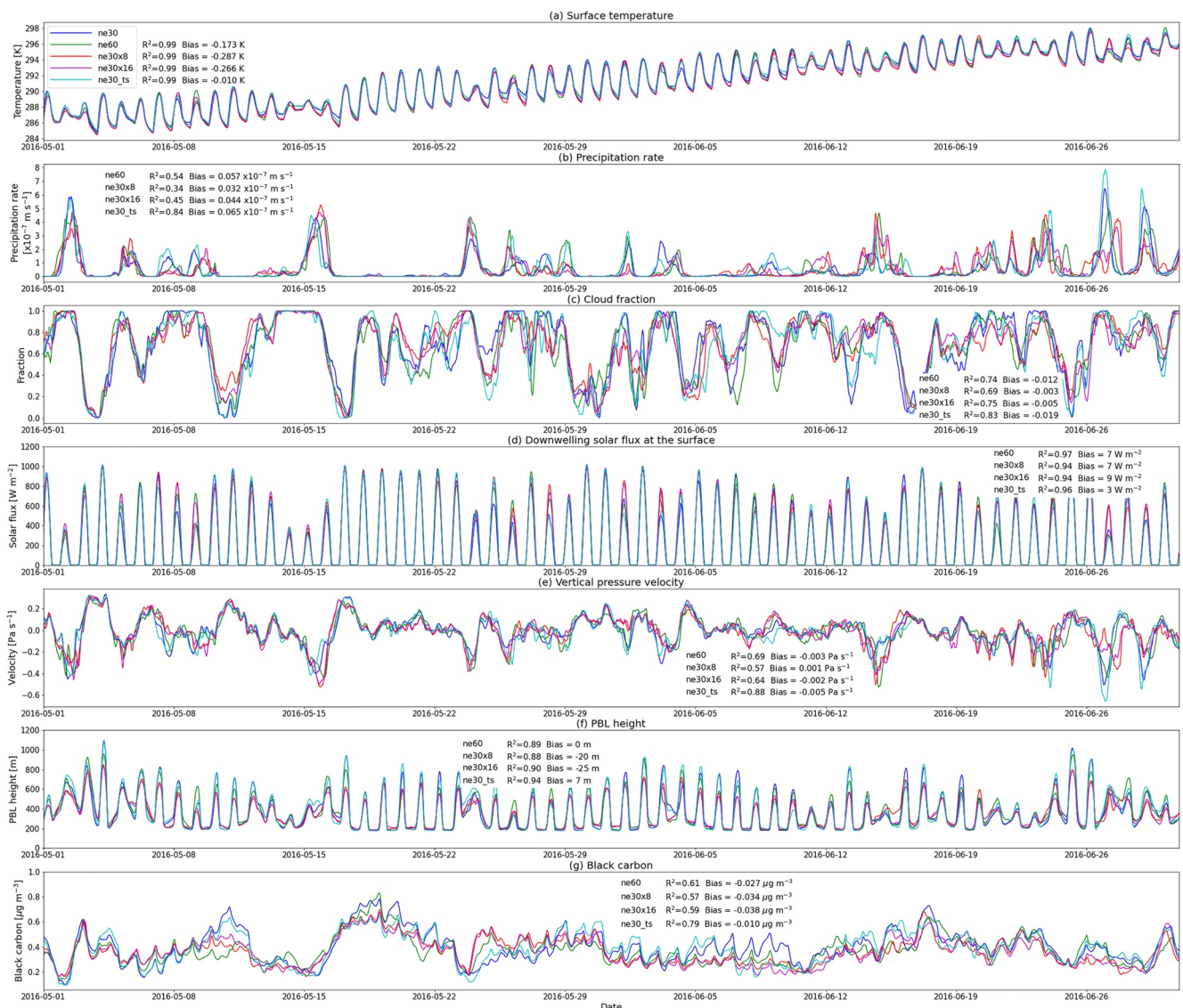
Figure 2. Domain (32°–40°N, 122–130°E) averaged time series of (a) surface temperature, (b) precipitation rate, (c) cloud fraction, (d) downwelling solar flux at the surface, (e) vertical pressure velocity at 500 hPa, (f) planetary boundary layer height, and (g) black carbon at the surface. Model results from ne30, ne60, ne30x8, ne30x16, and ne30_ts (ne30 but with the timestep for ne30x16 resolution) are shown in blue, green, red, purple, and cyan respectively. The coefficient of determination and mean bias are calculated against ne30 results.

model configurations, in terms of temporal variability. In general, the ne30 resolution with the ne30x16 timestep simulates the highest R^2 value and the lowest bias compared to the ne30 resolution. The best agreement is found for surface temperature, while the most inconsistent results are calculated for precipitation. Vertical velocities are also similar between model resolutions, as vertical grids are the same for all model configurations.

Spatial distributions of the variables in Figure 2 are presented in Figures S3–S8 in Supporting Information S1. Similar to temporal variability, the meteorological fields are largely consistent across different horizontal resolutions. On the other hand, there are notable local differences, particularly in coastal and mountainous regions, as high-resolution grids are capable of resolving regions with sharp geographical gradients (land/water or elevation). For instance, surface temperature (Figure S3 in Supporting Information S1) and PBL height (Figure S8 in Supporting Information S1) over the land and the ocean, which exhibit strong contrast in the high-resolution model simulations, are smoothed out in the low-resolution model simulations. The Taebaek mountain range is resolved in the regional refinement simulations, leading to significant local differences in the meteorological fields (surface temperature (Figure S3 in Supporting Information S1), downwelling solar flux (Figure S6 in
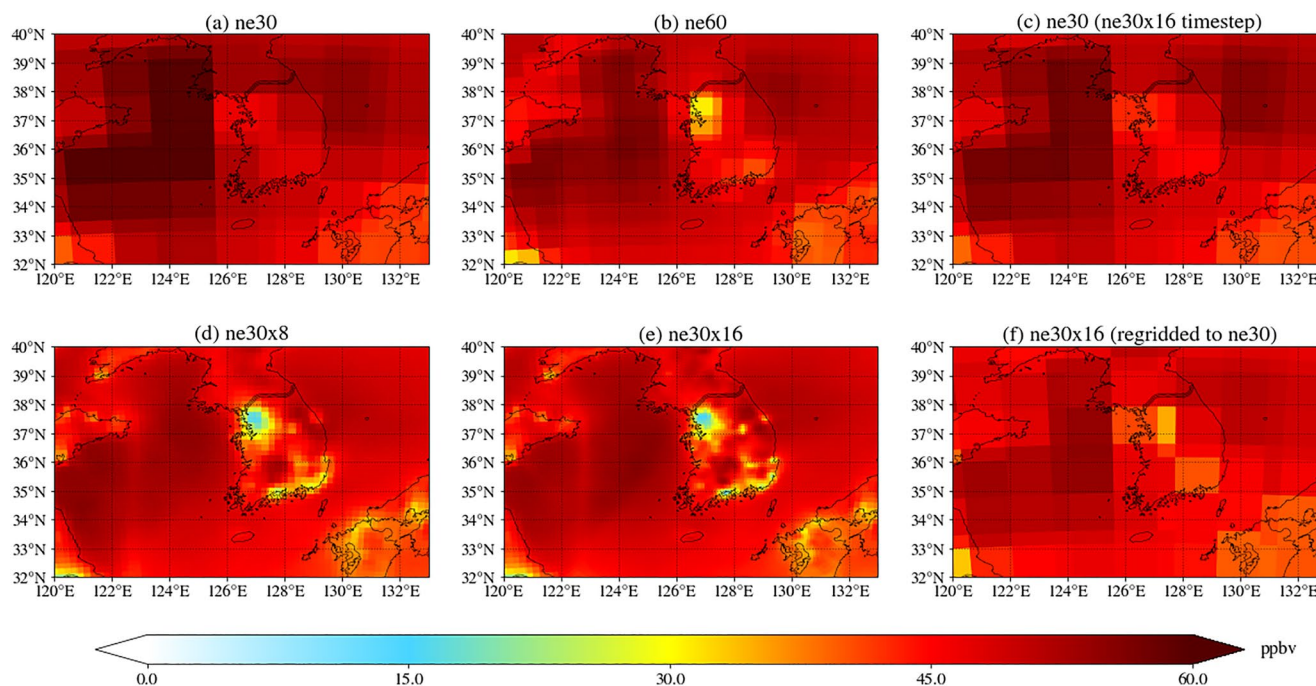
Figure 3. Simulated mean ozone mixing ratios at the surface (KORUS_D) in May–June 2016 on (a) global ne30 grid, (b) global ne60 grid, (c) global ne30 grid with ne30x16 timestep, (d) regional refinement ne30x8 grid, (e) regional refinement ne30x16 grid, and (f) ne30x16 but regridded to ne30. Units are ppbv. Note that grids are irregular (Section 2.2) and no interpolation is applied in the figure.

Supporting Information S1), and vertical pressure velocity (Figure S7 in Supporting Information S1)) over the eastern edge of the Korean peninsula. Comparisons with surface observations at two coastal and two mountainous sites suggest that high resolution simulations are generally more effective in reproducing local pressure, temperature, relative humidity, and wind speed (Figure S9 in Supporting Information S1).

Since various meteorological fields and chemical reactions simultaneously affect the concentration of chemical species, it is difficult to quantify the contribution of meteorological fields when calculating air quality changes due to regional refinement. Here we use BC at the surface to estimate the effects of meteorological fields on compounds, as BC is chemically inert but still affected by meteorological fields through wet deposition and vertical mixing. Similar to the meteorological variables, BC also shows some differences between model configurations in terms of temporal (Figure 2f) and spatial variabilities (Figure S10 in Supporting Information S1). However, normalized mean biases between grids are within 10% over the study domain and period, implying that BC changes due to precipitation and vertical mixing are generally small compared to the chemistry changes in Section 3.2.

3.2. Effects of Regional Refinement on the Chemistry Simulation

Figure 3 displays the average simulated ozone mixing ratio at the surface in May–June 2016 with four different grids and two additional results with different timesteps and regridding in the MUSICAv0 framework. The results from the two regional refinement grids (ne30x8 and ne30x16) show a clear decrease in ozone levels due to NO_x titration over urban areas, which is not captured by the ne30 grid as result of artificial mixing in the coarser resolution.

The left column in Figure 4 presents the diurnal variations of surface ozone and NO_x at the urban site, highlighting the substantial differences in NO_x levels between the grid resolutions, mainly due to the averaging of emission rates over larger areas in coarse grids. Despite relatively lower PBL height in the coarse grid (blue line in Figure 4i) that could increase NO_x levels during the day, this effect is not enough to offset the lower emission rates in the coarse grid. On the other hand, when the PBL simulated by the ne30x16 grid is regridded to the ne30 grid, it shows significantly lower PBL values (orange line in Figure 4i) due to Seoul's proximity to the coast and
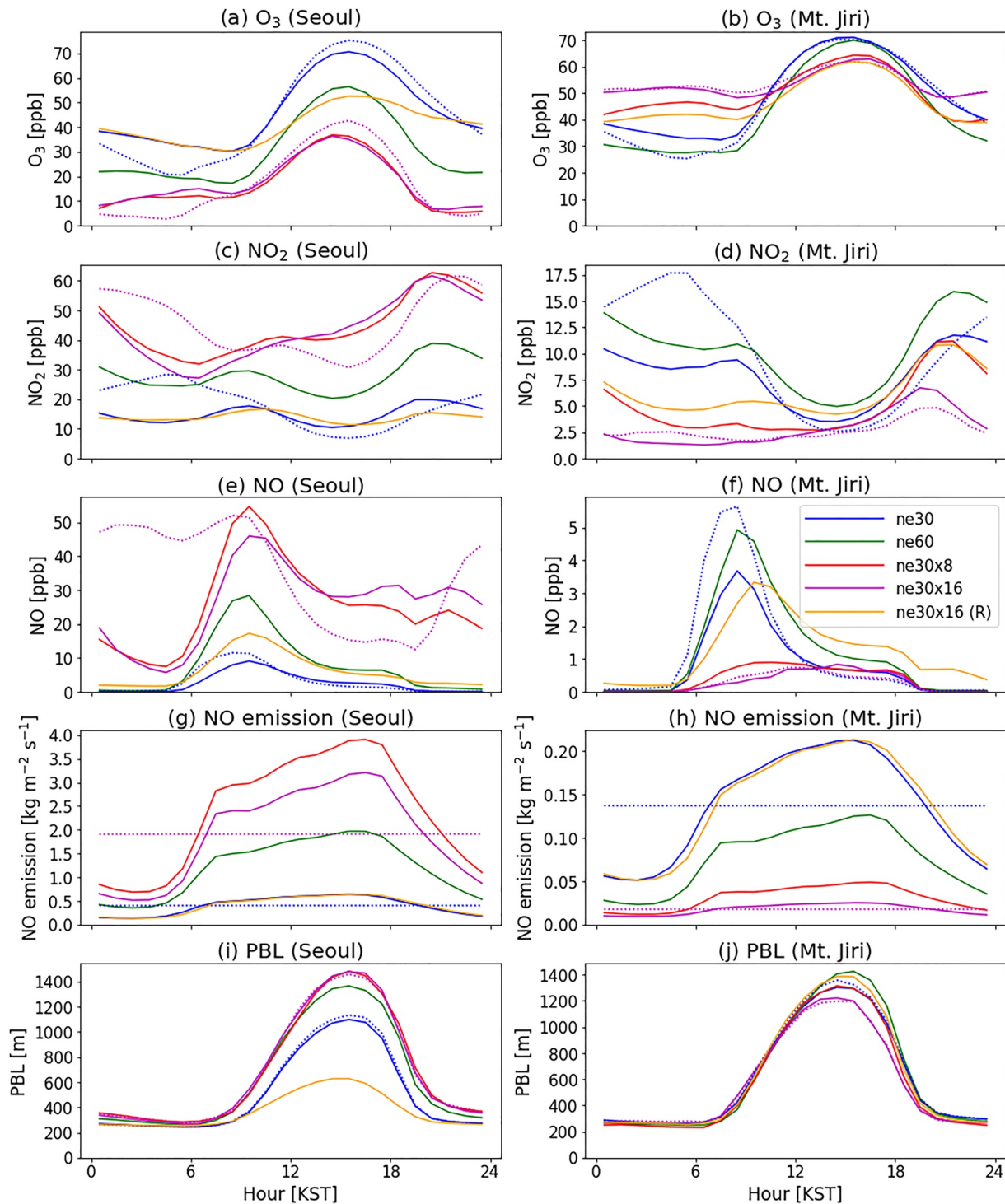
Figure 4. Diurnal variation of surface O_3, NO_2, and NO mixing ratios, NO emission flux, and planetary boundary layer (PBL) for urban (Seoul; 127.124°E, 37.522°N) and rural (Mt. Jiri; 127.731°E, 35.337°N) locations in South Korea (see Figure S11 in Supporting Information S1 for locations on the map). The different lines are colored according to the model grid resolution. Model results from KORUS_D (solid lines; the diurnal cycle of emission is applied) and KORUS_M (dotted lines; monthly emission) in May–June 2016 are used. Additionally, the ne30x16 (R) shows the KORUS_D ne30x16 results that are regridded to ne30 grids.
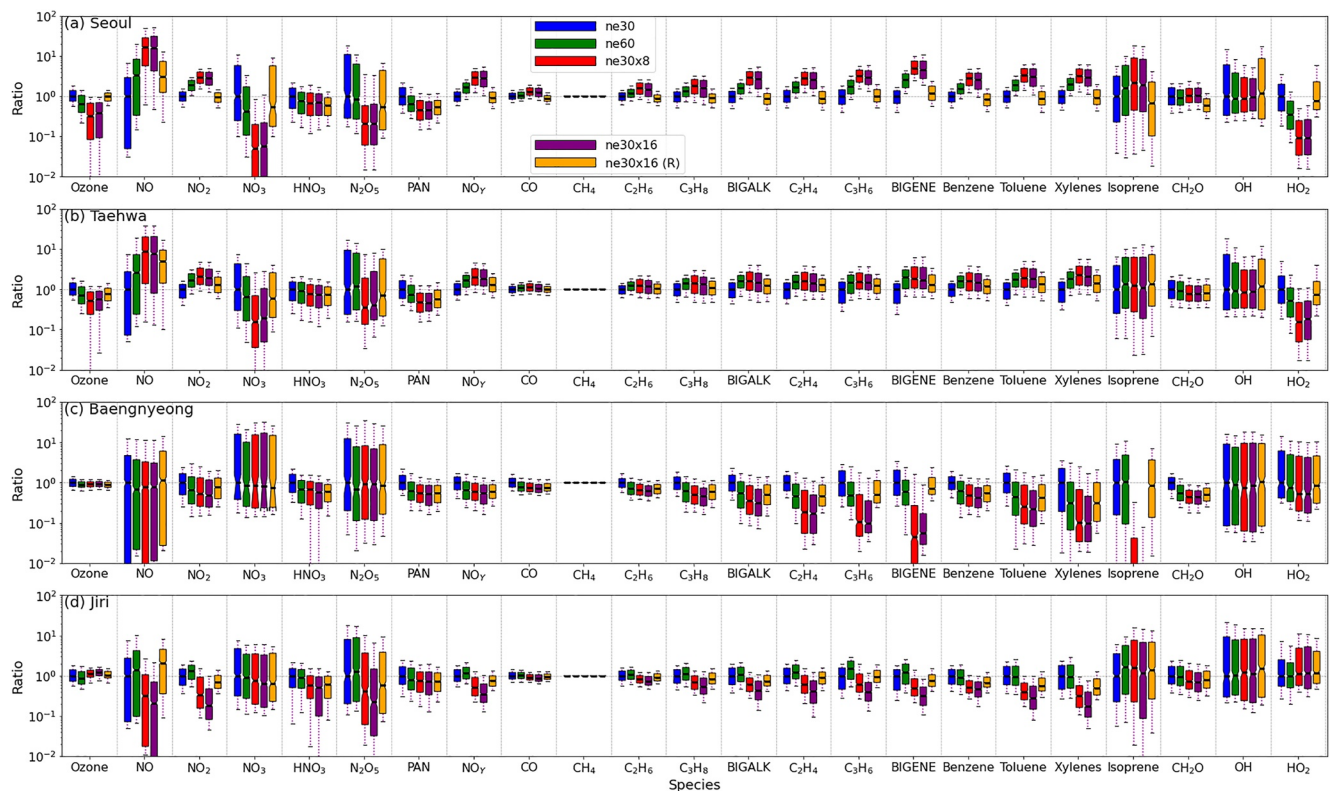
Figure 5. Box and whisker plots of simulated chemical species at the lowest layer of the model (KORUS_D; KORUSv5 emissions with diurnal cycle applied), which are normalized by the median value of each species in May–June 2016 simulated by ne30 resolution. Boxes and whiskers are calculated from the hourly output at (a) Seoul (127.124°E, 37.522°N), (b) Taehwa Forest (127.311°E, 37.312°N), (c) Baengnyeong Island (124.617°E, 37.950°N), and (d) Mt. Jiri (127.731°E, 35.337°N). Boxes show the 25th–75th percentile, with the black line showing the median. Whiskers represent the 10th and 90th percentiles. The ne30x16 (R) represents the ne30x16 simulations regridded to ne30 grids.

the dominance of ocean in the ne30 grid cell. It is even lower than the PBL simulated by the ne30 grid, indicating that physical parameter changes due to grid resolution are not linear as well.

The low ozone mixing ratios over urban areas (northwest and southeast in South Korea) in regional refinement grids increase when regridded to the ne30 resolution (Figure 3f), but remain lower than the ozone simulated by the ne30 grid (Figure 3a). Similar to the differences in meteorological fields (Section 3.1), there are no substantial differences in ozone due to timestep when compared to the changes caused by grid resolution.

The spatial distribution of ozone is shown to be related to the net chemical production rate of ozone as shown in Figure S12 in Supporting Information S1. The regional refinement grids exhibit net losses of ozone over urban areas. In addition, these high-resolution grids are capable of resolving the ship emission tracks over the Yellow sea, leading to a simulation of ozone loss due to concentrated ship emission plumes.

The changes in ozone over rural/mountain areas can also be attributed to misclassification of urban emissions in coarse grids. For example, the simulated NO and NO_2 levels at Mt. Jiri (rural) show substantial differences depending on the grid resolution (the right column in Figure 4), as nearby urban emissions are included in the coarse grids (ne30 and ne60). This causes nighttime ozone loss with differences of 10–20 ppbv between the model grids (Figure 4b). When the volume mixing ratios of ozone, NO, and NO_2 simulated by the ne30x16 grid are regridded to the ne30 grid (orange line in Figure 4), the results are closer to the volume mixing ratios simulated by the ne30 grid, but still differ due to nonlinear chemical reactions.

Figure 5 summarizes the distribution of chemical species simulated by different model grid resolutions, based on hourly output in May–June 2016. Four locations are chosen to represent a variety of air quality conditions: Seoul (urban), Taehwa Forest (urban downwind), Baengnyeong Island (continental outflow), and Mt. Jiri (rural/mountain). In addition to results from the four different grid resolutions, results from the ne30x16 resolution
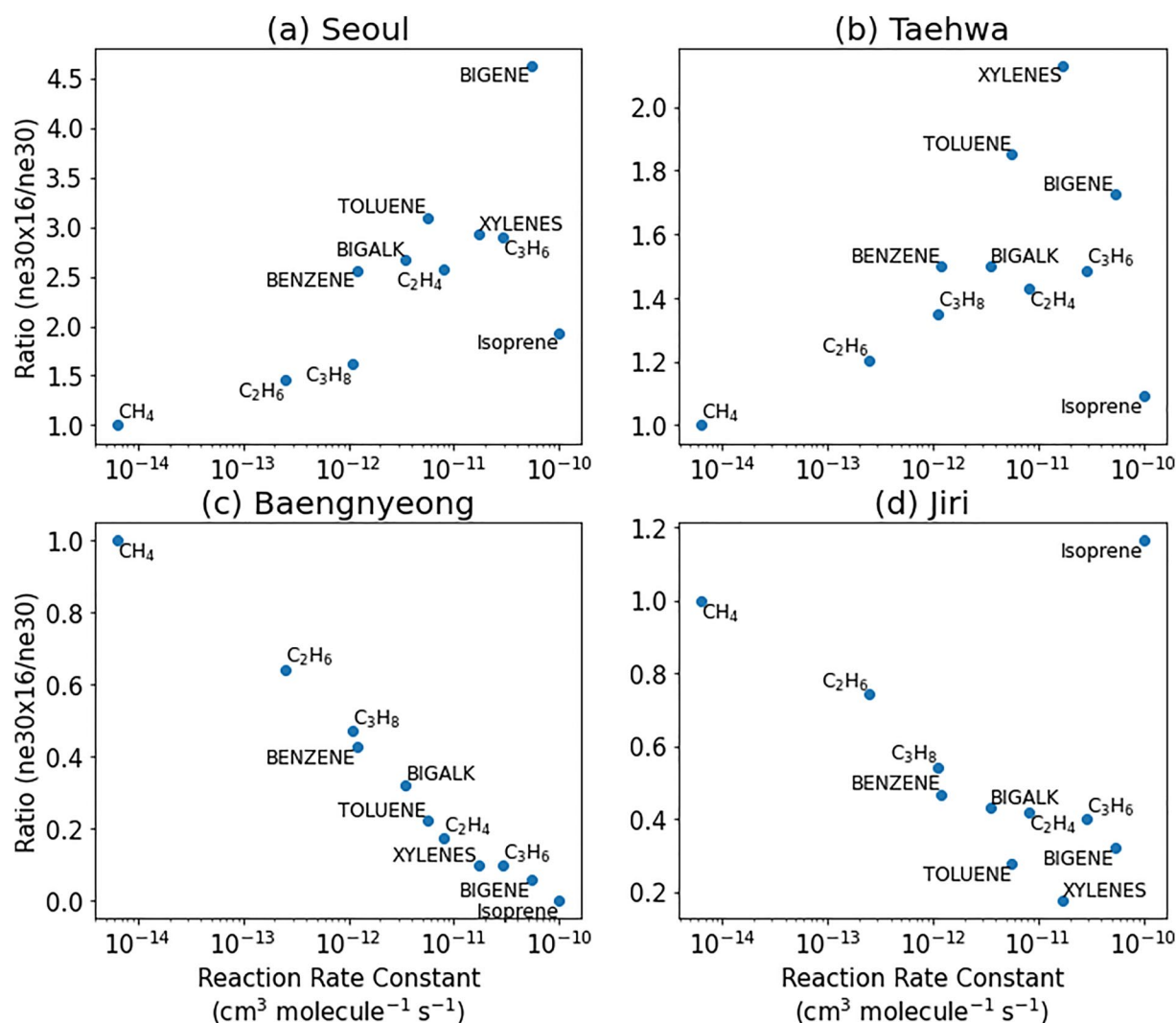
Figure 6. Scatterplots of the ratio of ne30x16 to ne30 versus reaction rate constant against OH at 298.15 K and 1,013.25 hPa for volatile organic compounds including CH_4, C_2H_6, C_3H_8, BIGALK (C ≥ 4 alkanes), C_2H_4, C_3H_6, BIGENE (C ≥ 4 alkenes), Benzene, Toluene, Xylenes (lumped xylenes), and Isoprene. The ratio is computed by dividing the simulated median value of ne30x16 by that of ne30 (KORUS_D; KORUSv5 emissions with diurnal cycle applied). The *x*-axis is on a logarithmic scale.

regridded to the ne30 grid (ne30x16 (R) in Figure 5) are also shown to distinguish between two main factors: grid representativeness and changes in chemistry/physics due to grid size and timestep. At Seoul, the ne30x16 resolution regridded to ne30 generally shows similar variability to the ne30 grid for all compounds, indicating that grid representativeness is more critical for the urban site. Conversely, at the remote sites, the variabilities of the ne30x16 regridded to ne30 results are more comparable to those of the ne30x16, implying that related changes in chemistry/physics are also important for downwind regions.

There are three primary factors contributing to differences in the simulation of chemical species caused by grid resolution. First, while the total emissions over the entire domain are the same, the emission flux at a specific location can vary. For example, the NO emission flux at Seoul (Figure 4g) and Mt. Jiri (Figure 4h) differ by a factor of 5. Second, lifetime plays a crucial role in understanding the dependence on grid resolution. As shown in Figure 6, the ratio of VOCs between the fine (ne30x16) and coarse (ne30) grid resolutions increases with the reaction rate constant against OH, suggesting that fine grid resolution becomes increasingly important for short-lived pollutants in regions with steep spatial gradients of chemical species. An exception is isoprene, particularly at Mt. Jiri, where the fine grid (ne30x16) resolves the mountain and the high isoprene emission flux. Although the relationship shown in Figure 5 weakens when the results of the ne30x16 are regridded to the ne30 grid resolution, it remains valid in the urban downwind (Taehwa) and continental outflow areas (Figure S13 in Supporting Infor-

mation S1). Third, secondary pollutants (e.g., ozone and formaldehyde) show less variation compared to primary pollutants. Secondary pollutants are formed through atmospheric oxidation over a period of time, making them less affected by the artificial mixing of emission plumes. For example, the lifetime of formaldehyde (~1.2 days against OH and ~4 hr against photolysis with overhead sun) is much shorter than that of benzene (~9.5 days against OH) and toluene (2.1 days against OH) (Atkinson & Arey, 2003) but there is smaller spread of model results for formaldehyde compared to benzene and toluene (Figure 5).

Among NO_z (NO_y minus NO_x) species, the grid resolution has a relatively minor impact on HNO_3 and PAN, but there are substantial differences in NO_3 and N_2O_5. NO_3 and N_2O_5 have strong diurnal variations due to their very short lifetime during the day (less than a minute), and their daytime concentrations are nearly zero. As a result, the peak nighttime concentrations of NO_3 and N_2O_5 are more effectively influenced by precursor concentrations from results with different grid resolution. Unlike VOCs, NO_3 and N_2O_5 are higher in the coarse grid (ne30) than in the fine grid (ne30x16). As shown in Figure S14 in Supporting Information S1, NO_3 and N_2O_5 show strong diurnal variation, with the greatest magnitude in the ne30 grid. These two species have similar diurnal profiles as they reach an equilibrium under typical tropospheric conditions (Wängberg et al., 1997). The major source of NO_3 is the reaction of NO_2 with O_3, with two major loss reactions: reaction with NO and photolysis (S. S. Brown & Stutz, 2012). In the urban atmosphere, the NO_3 + NO reaction rate exceeds the photolysis rate. For example, the reaction rate of NO_3 + NO (i.e., k[NO]) at Seoul is up to ~20 s^{-1} during the morning when NO is high in the ne30x16 grid simulation, while the photolysis rate for noontime conditions is ~0.2 s^{-1} (Orlando et al., 1993). Due to higher nighttime O_3 in the ne30 grid compared to other grids (Figure 4a; up to seven times), the NO_3 production rate is higher in the ne30 grid simulation (Figure S15 in Supporting Information S1). On the other hand, the low NO mixing ratio due to artificial dilution in the ne30 grid results in a low loss rate of NO_3 (Figure S15 in Supporting Information S1). The results of the ne30x16 regridded to ne30 do not match those of the ne30 grid for nitrogen compounds and ozone. For example, NO at Mt. Jiri during the nighttime clearly shows nonlinearity: when NO simulated by the ne30x16 is regridded to the ne30 grid, it shows 10–20 times higher NO than other grids because of mixing with the nearby industrial city (Gwangyang, <50 km from Mt. Jiri) where NO is very high due to concentrated emissions and low ozone during the nighttime (Figure 4f). The original ne30 grid includes both Mt. Jiri and Gwangyang in one grid point and the NO emitted over the industrial city is relatively quickly converted to NO_2 due to abundant ozone during the nighttime. Overall, these differences in O_3, NO, and NO_2 cause differences in NO_3 and N_2O_5 concentrations.

The behavior of HO_x species also differs based on the grid resolution used in the simulation (Figure S16 in Supporting Information S1). On average, HO_x concentrations are lower in simulations using a fine grid resolution compared to those using a coarse grid resolution. This is due to a combination of factors, including the lower daytime ozone levels simulated by the fine grid, which limits the production of OH through ozone photolysis (Brasseur et al., 1999), as well as the lower OH reactivity (i.e., loss rate) in the fine grid. Therefore, daytime ozone is important for OH production, and the coarse grid simulates higher daytime ozone in urban areas (Figures 3 and 4). For example, the OH reactivity over Seoul is 9.8 s^{-1} in the coarse grid (ne30) compared to 24.8 s^{-1} in the fine grid (ne30x16) (Figure 7 and Figure S17 in Supporting Information S1). Higher production rates and lower loss rates together result in higher HO_x concentrations in Seoul. HO_x concentrations at Mt. Jiri also vary according to the grid resolution (Figures S16b and S16d in Supporting Information S1). During the early morning (6–9 a.m.), OH in the ne30x16 grid is higher due to the higher production of OH from ozone photolysis. Conversely, HO_2 in the coarse grid is suppressed due to higher NO (Figure 4f) via the reaction of HO_2 with NO (Stone et al., 2012). During the daytime, OH is low in the fine resolution grid due to the strong diurnal variations in OH reactivity resulting from isoprene emissions (Figure S17d in Supporting Information S1). Although these differences are localized, they are comparable to the inter-model spread in OH (Zhao et al., 2019).

Different OH, O_3, and NO_3 concentrations can lead to different fractions of the initial pathways of VOC reactions, as well as further oxygenated VOCs and the chemical characteristics of secondary organic aerosols (SOA). For example, organic nitrates are the major products of VOC reactions with NO_3, which have significant impact on regional NO_x, O_3, and SOA (Pye et al., 2010; Schwantes et al., 2015). The initial pathways of VOC reactions are substantially different based on the grid resolution as shown in Figure S18 in Supporting Information S1, especially during the nighttime. The ne30 grid simulates that 90% of monoterpenes at around midnight react with NO_3, while this fraction decreases to 65% in the ne30x16 grid simulation for the KORUS_D case. It is important to note that the vertical resolution is the same for all simulations in this study (~120 m at the bottom layer). Increasing the vertical resolution in the boundary layer, which is being actively developed for the next
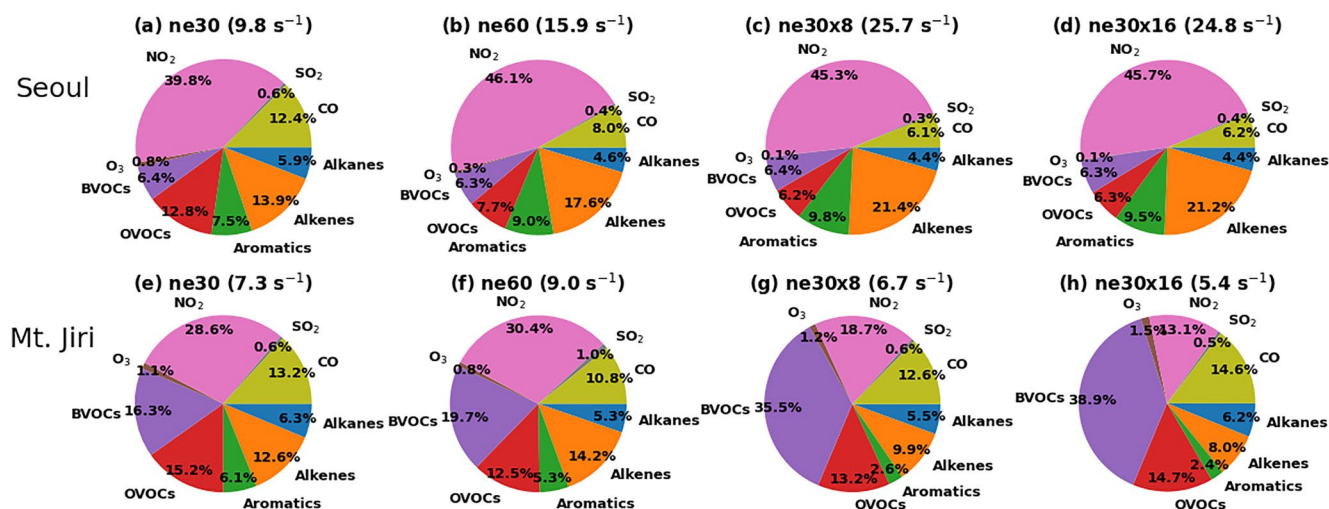
Figure 7. Pie charts showing relative contributions to OH reactivity at Seoul (a, b, c, d) and Mt. Jiri (e, f, g, h) at the surface (KORUS_D; KORUSv5 emissions with diurnal cycle applied). The total OH reactivity is shown in parentheses. Trace gases used in the calculation are available in Table S1 in Supporting Information S1.

version of CESM, can also affect the VOC reaction pathways especially during the nighttime conditions (Menut et al., 2013). Future studies with enhanced horizontal and vertical resolutions will be needed to investigate the changes in oxidants, organic nitrates, and the fate of the nitrogen compounds.

### 3.3. Effects of Anthropogenic Emission Inventory on the Simulation

There are a number of anthropogenic emission inventories that have been utilized in chemistry models (Elguindi et al., 2020). As shown in Table 1, the degree of agreement between emission inventories can vary depending on the species. In order to assess the impact of the emission inventory on air quality simulation, three factors were considered in this study: differences between inventories, the diurnal cycle of emissions, and the speciation of NO_x. These factors are compared with the resolution effect to determine their relative significance.

Most anthropogenic emission inventories are provided in monthly or yearly increments. As a result, some models incorporate diurnal variation into their simulations through the use of diurnal scaling factors applied to certain species (Park et al., 2021). For example, the Harmonized Emission Component (HEMCO), which was originally developed for the GEOS-Chem model, applies hourly scale factors to anthropogenic emissions (Keller et al., 2014; Lin et al., 2021). Meanwhile, other global chemistry models such as CAM-chem (Emmons et al., 2020) and GFDL AM4.1 (Horowitz et al., 2020) have used monthly anthropogenic emissions without imposing diurnal variation.

Many anthropogenic emission inventories do not provide further speciation of NO_x emissions into NO and NO_2 with only a few regional emission inventories providing such information (e.g., the KORUSv5 emission inventory used in this study). As a result, global chemistry models generally assume NO_x as NO when emitting NO_x emissions. This approximation is adequate for coarse grids where emissions are instantly diluted into large areas, but may not be appropriate for high-resolution grids. For example, CAM-chem emits NO_x as NO except for aircraft emissions (emitted as NO_2) (Emmons et al., 2020). Similarly, GEOS-Chem emits NO_x as NO except for some regional inventories (e.g., National Emissions Inventory, DICE-Africa) that provide both NO and NO_2 information. On the other hand, the Weather Research and Forecasting model coupled with Chemistry (WRF-chem), a regional chemistry model, speciates NO and NO_2 using an input emission processing tool. As global chemistry models move toward finer grid resolution (Bindle et al., 2021; Pfister et al., 2020), the speciation of NO_x can become important and is discussed further below.

To summarize the results from various simulations, we present Taylor diagrams (Figure 8 and Figures S19–S23 in Supporting Information S1) and calculate the normalized mean root mean square error (NRMSE; Tables S2 and S3 in Supporting Information S1). The NRMSE is calculated as

$$\text{NRMSE}_{\text{case}} = \frac{1}{\sigma} \sqrt{\frac{\sum_{i=1}^{N} (M_{\text{case},i} - M_{\text{ref},i})^2}{N}} \tag{1}$$
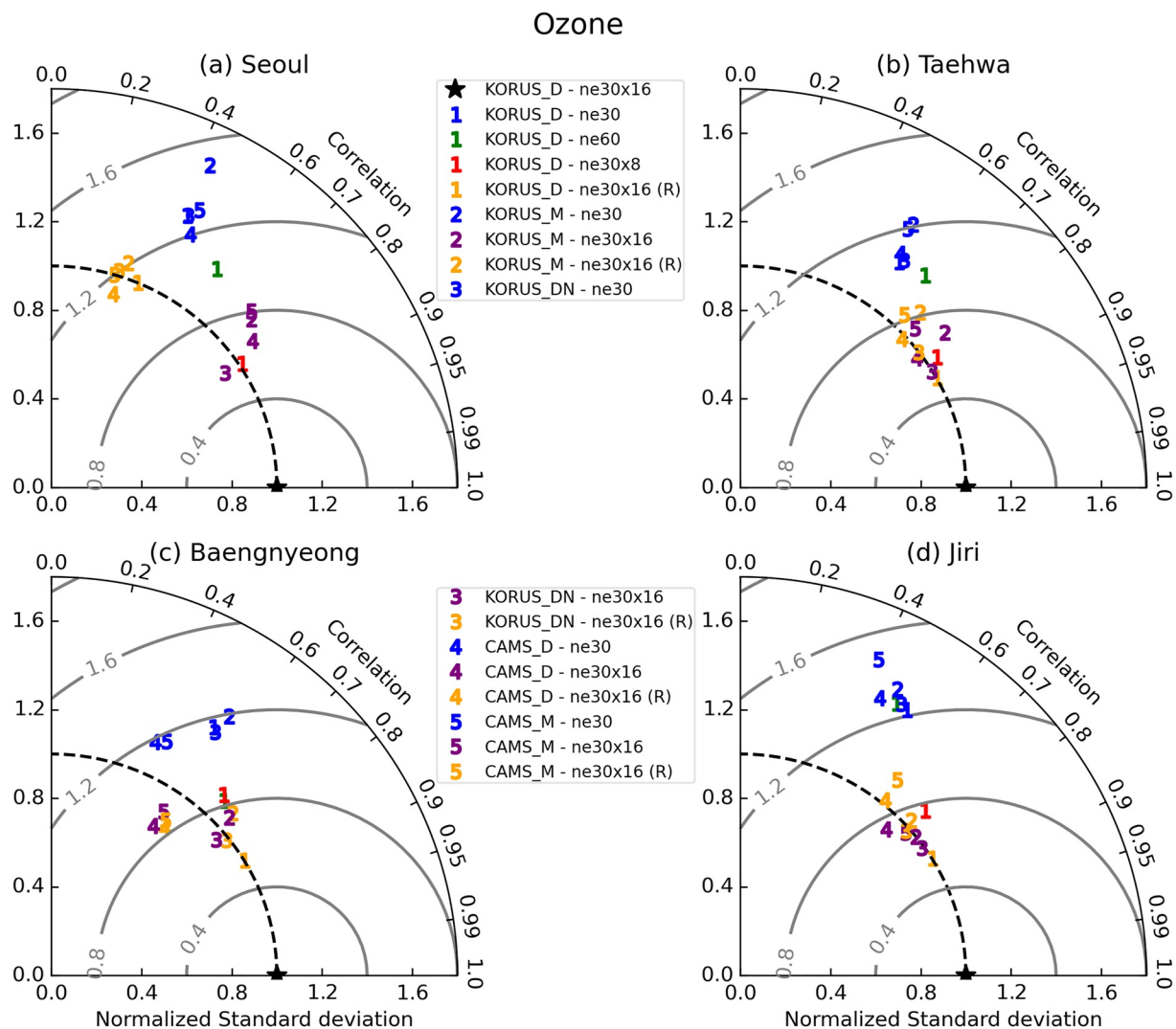
Ozone

Figure 8. Taylor diagrams summarizing the comparison of hourly ozone in May–June 2016 at the surface by different simulations (represented by number symbols) and grid resolutions (represented by colors). The ne30x16 (R) represents the ne30x16 simulations regridded to ne30 grids. The reference point (star symbol) corresponds to the ozone simulated by KORUS_D (ne30x16). Correlation is on the angular axis and the normalized standard deviation is on the radial axis.

where M_{case} and M_{ref} are model results and *ref* is the reference case (KORUS_D ne30x16). N is the total number of points, based on hourly concentrations in May–June 2016. Here we use the standard deviation (σ) for normalization, but there are also other factors that can be used, including mean, max–min, and the interquartile range (Otto, 2019). It is worth noting that the NRMSE can change by up to three orders of magnitude with different scale factors, therefore, the analysis is performed in terms of relative comparison between simulations. In addition, normalized mean biases are also calculated in Table S4 in Supporting Information S1 to show the mean differences between simulations.

In Figure 8, Taylor diagrams are presented at four locations for surface ozone. The KORUS_D ne30x16 case has been selected as the reference because it has the finest resolution, as well as region-specific emissions with diurnal cycles and NO_x speciation. The distance of each point from the reference point represents the RMSE of each model case compared to the KORUS_D ne30x16 simulation. The spread of points in the diagram is proportional to the difference each element makes in the simulation. Among the various factors discussed, grid resolution, indicated by different colors, has the biggest impact on the differences between simulations. The regridding of ne30x16 results to the ne30 grid (orange color) does not decrease the distance from the reference point at Seoul. This highlights the non-linear nature of chemistry changes caused by grid resolution. In contrast, the regridded ne30x16 results to ne30 display similar distributions to the ne30x16 grid results over rural areas, despite having high normalized mean biases (Table S4 in Supporting Information S1).

The diurnal cycle of emission is another important factor especially for urban regions. In the Taylor diagrams presented in Figure 8 and Figures S19–S23 in Supporting Information S1, it can be seen that the CAMS_D simulations (CAMSv5.1 inventory with diurnal cycle applied, marked as 4) are closer to the reference point compared to KORUS_M simulations (KORUSv5 inventory without the diurnal cycle of emissions, marked as 2) in some cases, indicating that the diurnal cycle of emissions can play a more significant role than the emission inventory. However, the significance of the diurnal cycle varies depending on the species. The grid resolution is the main factor that influences the simulation of secondary species without strong diurnal variation, such as formaldehyde (as shown in Figure S21 in Supporting Information S1). As expected, the impact of the diurnal cycle decreases as chemical tracers move away from the emission source. This is evident as urban and downwind-of-urban regions show more spread than oceanic and mountainous regions.

The diurnal cycle of emissions has a significant impact on nighttime ozone levels in the urban areas (dashed line in Figure 4a). The inclusion of a diurnal cycle on emissions leads to higher ozone levels due to lower NO_x emissions at night (Figure 4g). The diurnal profile of emission rates also affects daytime concentrations of OH and HO_2 (Figures S16a and S16c in Supporting Information S1), resulting in changes to ozone and OH reactivity (Figure S17a in Supporting Information S1). The inclusion of the diurnal cycle leads to changes in OH, O_3, and NO_3, which in turn alter the reaction pathways of initial VOC oxidation, as shown in Figure S18 in Supporting Information S1. For example, the NO_3 fraction changes from 50% (panel f) to 65% (panel d) at midnight after the diurnal profile is applied to emissions in the ne30x16 grid simulation. The diurnal cycle makes a significant contribution to the VOC reaction pathways for the ne30x16 grid simulation, whereas no substantial changes have been found for the ne30 grid (panels a and e in Figure S18 in Supporting Information S1).

The findings are further supported by the NRMSE values in Tables S2 and S3 in Supporting Information S1 for a wide range of chemical species. Applying diurnal cycles significantly changes the results over urban areas but these changes decrease as the chemical environment becomes less polluted. The largest factor affecting simulations in terms of NRMSE is grid resolution in terms of NRMSE. However, the difference between the ne30x8 and ne30x16 results is smaller than other factors. For instance, the NRMSE values of the KORUS_D ne30x8 are generally smaller than those of the ne30x16 grid simulation for other cases (KORUS_M, CAMS_D, and CAMS_M), indicating that changes caused by other factors are larger than changes resulting from the grid resolution switch from ne30x16 to ne30x8. The one exception is the KORUS_DN (KORUSv5 inventory with all NO_x emitted as NO) ne30x16 simulation which shows similar NRMSE values compared to KORUS_D ne30x8. Both KORUS_D ne30x8 and KORUS_DN ne30x16 also exhibit the lowest biases compared to other simulation cases (Table S4 in Supporting Information S1). As shown in Taylor diagrams which show no significant difference between the KORUS_D and KORUS_DN simulations, the assumptions that all NO_x emissions are emitted as NO are still valid at the highest resolution (ne30x16) even for nitrogen species that are directly influenced by NO_x speciation.

NRMSE values from the ne30x16 regridded to ne30 are generally in between the original ne30 and ne30x16 NRMSE values, implying that both artificial mixing and chemistry changes upon dilution affect the simulation results (ideally, ne30 and ne30x16 regridded to ne30 results should show the same results when there is only artificial mixing effect). The NRMSE difference between ne30 and ne30x16 regridded to ne30 is smaller for urban areas than for rural areas. This tendency shows that artificial mixing is more important for urban areas while the associated chemistry change is more important for rural areas.

The differences in emission inventory can have a significant impact on the simulation of some VOCs where the emission amounts are significantly different in different inventories. For example, the simulation of toluene using the KORUSv5 inventory on ne30 grids shows similar or lower NRMSE values compared to those using the CAMSv5 inventory on ne30x16 grids over Seoul and Taehwa due to a factor of 7 difference in toluene emission between the two inventories in South Korea (Table 1). This also holds true for C_2H_6 and C_3H_8 with a factor of 2 emission differences between the inventories. On the other hand, the NRMSE by the CAMS_M (CAMSv5 without diurnal cycle emissions) ne30x16 simulation is lower than the NRMSE by KORUS_D (KORUSv5 with diurnal cycle of emissions) ne30 for benzene, as the emission differences are within 50% for South Korea. Given the large discrepancies that exist among VOC emission estimates (Li et al., 2021), it is important to have the most up-to-date information on not just the total NMVOC but also VOC speciation for regional chemistry modeling.

The results of the study highlight the simultaneous impact of various factors on the model outcomes, particularly the significance of grid resolution and the diurnal cycle of emissions. However, for some VOCs with substantial differences in emission amounts between inventories, the discrepancies between the emission inventories have a

greater impact on the model results. Allocating all NO_x emissions to NO does not result in significant changes to the model results, even at the highest resolution (ne30x16), and remains a valid assumption for regional refinement grids in South Korea. The factors studied in this work are more prominent in urban environments, particularly with regard to grid resolution. Hence, when evaluating atmospheric chemistry models against observations from urban sites, it is necessary to consider the impact of grid resolution to avoid significant biases.

3.4. Biogenic Emissions by Different CLM Configurations and Grid Resolutions

Biogenic emissions in state-of-the-art chemistry models are calculated online using the meteorological fields within the model at each time step, with many using the MEGAN algorithm (Guenther et al., 2006, 2012). The MEGAN v2.1 in MUSICAv0 uses temperature, light, and other parameters for each time step from the land model (CLM5) to estimate the emission flux of biogenic VOCs. Therefore, the amounts of biogenic emissions can be impacted by differences in meteorological fields resulting from different grid resolutions. Furthermore, vegetation state variables (e.g., LAI) can be calculated prognostically or prescribed in CLM5, which can also affect biogenic emissions. In this section, we compare isoprene emissions calculated from different CLM configurations and grids.

Figure 9 shows the isoprene emission flux at the surface simulated by MEGAN v2.1 using two different CLM configurations and grids. The isoprene emissions during May–June 2016 over the region of 125°E–130°E and 34°N–38°N are 73.8 and 72.9 Gg for the ne30 and ne30x16 grids with prescribed LAI (SP), and 84.2 and 70.1 Gg with prognostic LAI (BGC). Given that the uncertainty in isoprene emission is about a factor of two (Guenther et al., 2012), the differences are small regardless of grid resolution and prognostic LAI option.

However, the underlying mechanism behind the isoprene emissions could be different. As shown in Figure S24 in Supporting Information S1, GAMMA (emission activity factor) with the BGC is 52% higher than that with the SP, which is mainly due to the differences in LAI (Figure S24c in Supporting Information S1). This is expected as the main difference between the two CLM5 configurations is whether LAI is calculated or prescribed. Although isoprene emission is proportional to LAI (Guenther et al., 2012), the simulations show that the specific LAI corresponding to a particular plant functional type (PFT) is important, not just the total LAI. Broadleaf trees have at least an order of magnitude higher isoprene emission factors compared to needleleaf trees, grasses, and crops. For example, broadleaf deciduous temperate trees emit isoprene at a rate of 10,000 μg m^{-2} h^{-1} while needleleaf evergreen temperate trees emit only 600 μg m^{-2} h^{-1}. As shown in Figure S25 in Supporting Information S1, both SP and BGC have similar broadleaf tree LAI, resulting in similar isoprene emissions between SP and BGC despite substantial differences in total LAI.

This is not the case for all biogenic compounds, as the emission factors vary based on the chemical species. For example, the emission factor of CO is the same (600 μg m^{-2} h^{-1}) across all PFTs, and the ne30x16 BGC calculates 48% higher biogenic CO emissions than ne30x16 SP (Figure S26 in Supporting Information S1), which is similar to the changes in the total GAMMA (52%). Therefore, not only the total LAI (e.g., CO) but also the accurate representation of PFTs (e.g., isoprene) is crucial for calculating realistic biogenic emissions. To utilize the biogeochemistry option for prognostic vegetation state in MUSICA or CESM, future studies will need to evaluate the LAI for each PFT or the emission of individual biogenic species.

4. Comparison With Observations

In this section, we compare the model results with observations collected during the KORUS-AQ field campaign in May–June 2016 (Crawford et al., 2021). For the comparison, we extract the closest model grid point to the aircraft position at each minute of the flight. As the flight routes encompass a wide range of environments, including urban and rural areas in South Korea, the Yellow Sea, and the free troposphere, with abundant observations available at each location and time, we categorize the flight paths into different regions. We also include two additional ground observations to complement the airborne observations, because the aircraft cannot collect data near the surface, except during missed approaches, and the aircraft observations are available during the daytime only.

4.1. Aircraft Measurements

We evaluate the modeled temperature and wind speed (Figure S27 in Supporting Information S1). Despite the difference in nudging applied for global and regional refinement grids (Section 2.1), all model cases effectively reproduce the observed temperature and wind speed profiles over South Korea. For a few cases, such as wind
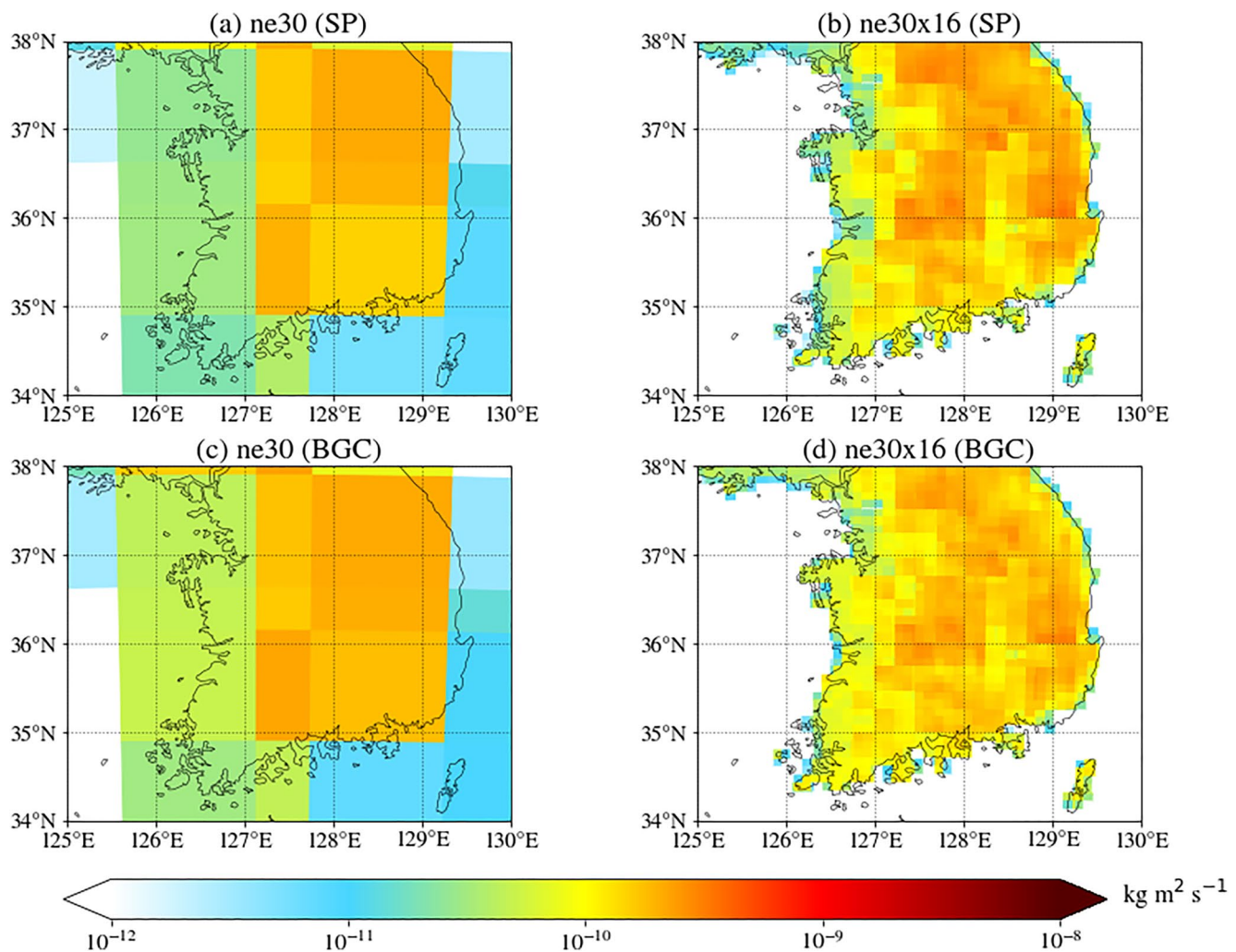
Figure 9. Isoprene emissions at the surface (KORUS_D (a, b) and KORUS_BGC (c, d)) in May–June 2016 on (a, c) the global ne30 grid, and (b, d) the regional refinement ne30x16 grid. Unit is kg m^{-2} s^{-1}.

speed at 6–7 km altitude over the Yellow Sea, the simulated values are biased but the values simulated by all model cases yield similar simulations.

Figure 10 represents the comparison of the MUSICAv0 simulations to the NO and NO$_2$ measurements from the DC-8. The median values of the model are usually within the interquartile range of the observations. However, the evaluation statistics can vary significantly depending on the grid resolution and emission inventory. The high-resolution grids produce better results, particularly for the Seoul Metropolitan Area (SMA) and the Yellow Sea, while the ne30 grid fails to reproduce low NO$_x$ over the Yellow Sea or high NO$_x$ over the SMA. The ne30 grid instantly spreads emissions from ships to wider areas, leading to NO$_x$ overestimation over the Yellow Sea, for flight paths that did not fly near ships. The mean biases of NO$_x$ during the entire campaign are −28% and 19% for the ne30 and ne30x16 grids, respectively, indicating slight improvements in the high-resolution simulation. The choice of emission inventory is less crucial except for the ne30 grid over the Yellow Sea as NO$_x$ emissions are similar between the two inventories (Table 1). The diurnal cycle does not play a role in the difference for the entire campaign average, as its effect is larger during nighttime (Section 3.2) than during the day.

The simulations show an overestimation of HNO$_3$ and an underestimation of peroxyacetyl nitrate (PAN) (Figure 10), regardless of the model resolution and emission inventory used. Although the ne30x16 grid provides slightly better results for HNO$_3$ results when comparing the median values (Figure 10i), the mean bias remains almost the same (198% and 196%) for both ne30 and ne30x16 grids. This overestimation of HNO$_3$ is also found
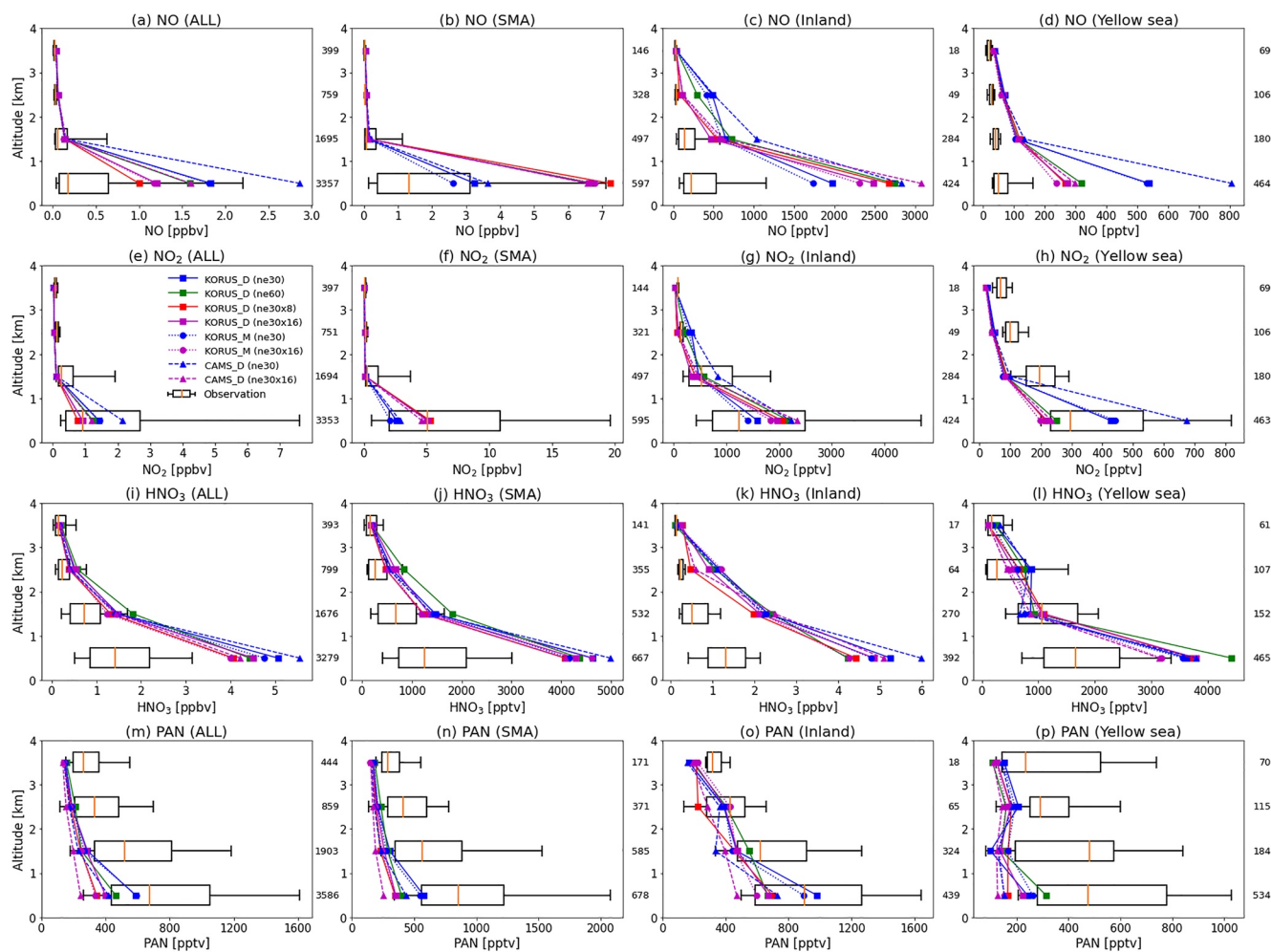
Figure 10. Vertical profiles of NO (a, b, c, d), NO_2 (e, f, g, h), HNO_3 (i, j, k, l), and PAN (m, n, o, p) over the Korea-United States Air Quality (KORUS-AQ) flight tracks for four regions, the whole campaign ("ALL"), the Seoul Metropolitan Area ("SMA," 37.0°N–37.6°N, 126.6°E–127.7°E), Inland South Korea ("Inland," 35.0°N–37.0°N, 127.0°E–129.0°E), and the Yellow Sea (30.0°N–38.0°N, 123.0°E–125.0°E). The regions defined in this plot are shown in Figure S11 in Supporting Information S1. Note that the Yellow Sea is narrowly defined to exclude the Daesan industrial region where substantial underestimation of volatile organic compound emission was reported (Fried et al., 2020). Profiles are grouped into 1 km bins. Box boundaries show the measured 25th–75th percentile with the middle orange bar showing the median from the aircraft observations. Whiskers show the 10th and 90th percentiles of aircraft measurements. The model median values from the three simulations are plotted—KORUS_D (KORUSv5 with diurnal cycle applied to emissions; square, solid line), KORUS_M (KORUSv5 without diurnal cycle of emissions; circle, dotted line), and CAMS_D (CAMSv5.1 with diurnal cycle applied to emissions; triangle, dashed line), for ne30 (blue), ne60 (green), ne30x8 (red), and ne30x16 (purple) grid resolutions. The number of data points in each kilometer interval is shown at the right of each panel. Plots are limited to 4 km altitude to highlight the boundary layer comparison.

in the multi-model comparison results reported by Park et al. (2021). The good agreement between the modeled NO_2 and OH values and the observations (Figures 10 and 11; respective mean biases of −25% and 10% for ne30 and ne30x16 grids for NO_2, and 39% and 23% for OH) suggest that the overestimation of HNO_3 could be caused by loss processes not accounted for, such as HNO_3 uptake on coarse mode aerosols (Hrdina et al., 2021). The underestimation of PAN was also found by the KORUS-AQ model intercomparison study (Park et al., 2021). The discrepancy between the model and observations is attributable to the underestimation of its precursors, as shown in Figure S28 in Supporting Information S1 for acetaldehyde and ethane.

The results for OH and HO_2 also vary depending on the horizontal resolution and emission inventory (Figure 11). OH is slightly overestimated and HO_2 is slightly underestimated, with improved results seen in the high-resolution models particularly over the SMA. The differences in OH over the SMA at the lowest altitude bin, which can range up to 84% depending on the grid resolution, are comparable to the variations found among global chemistry models (Nicely et al., 2017). As OH has a significant impact on the lifetime of chemical species and their trans-
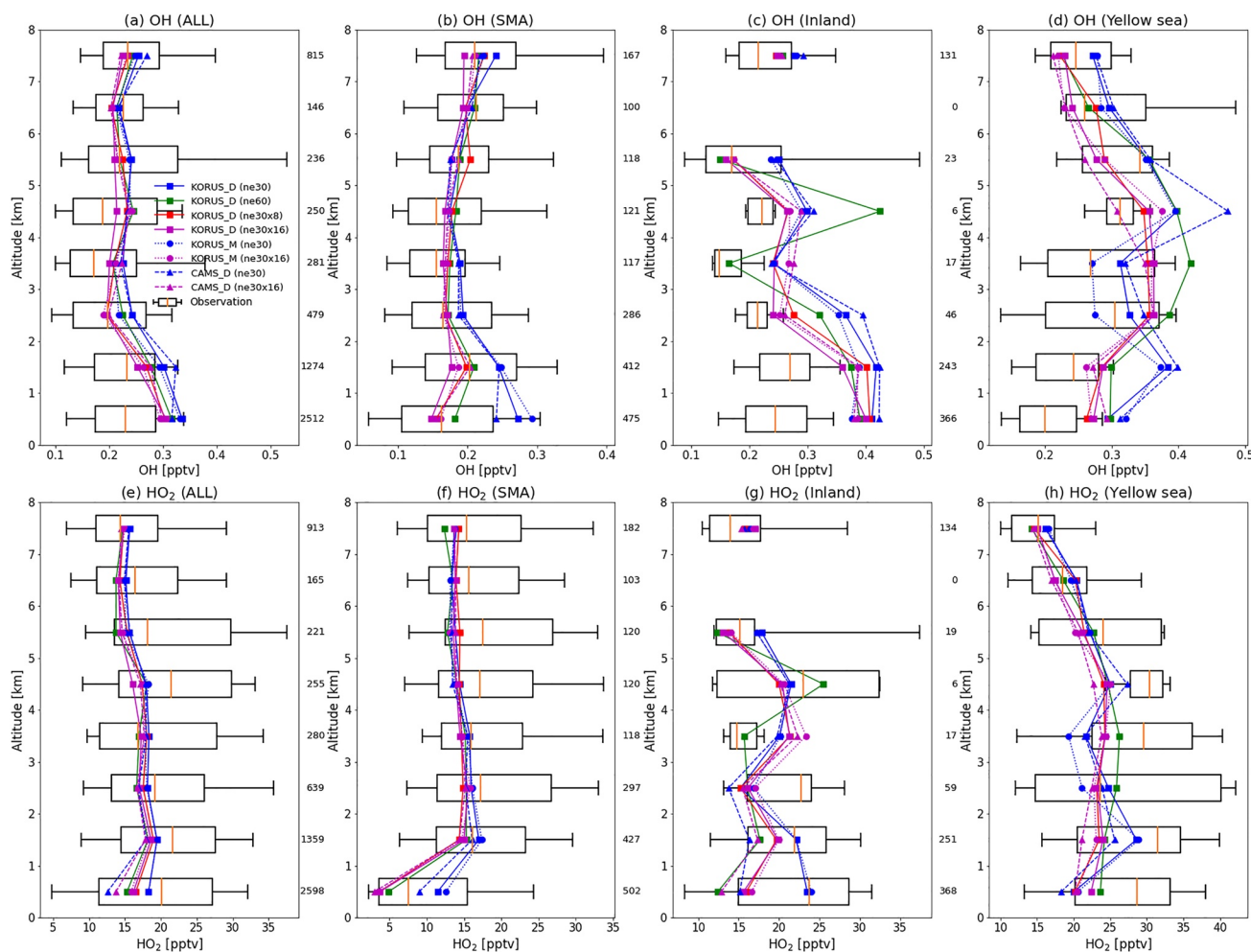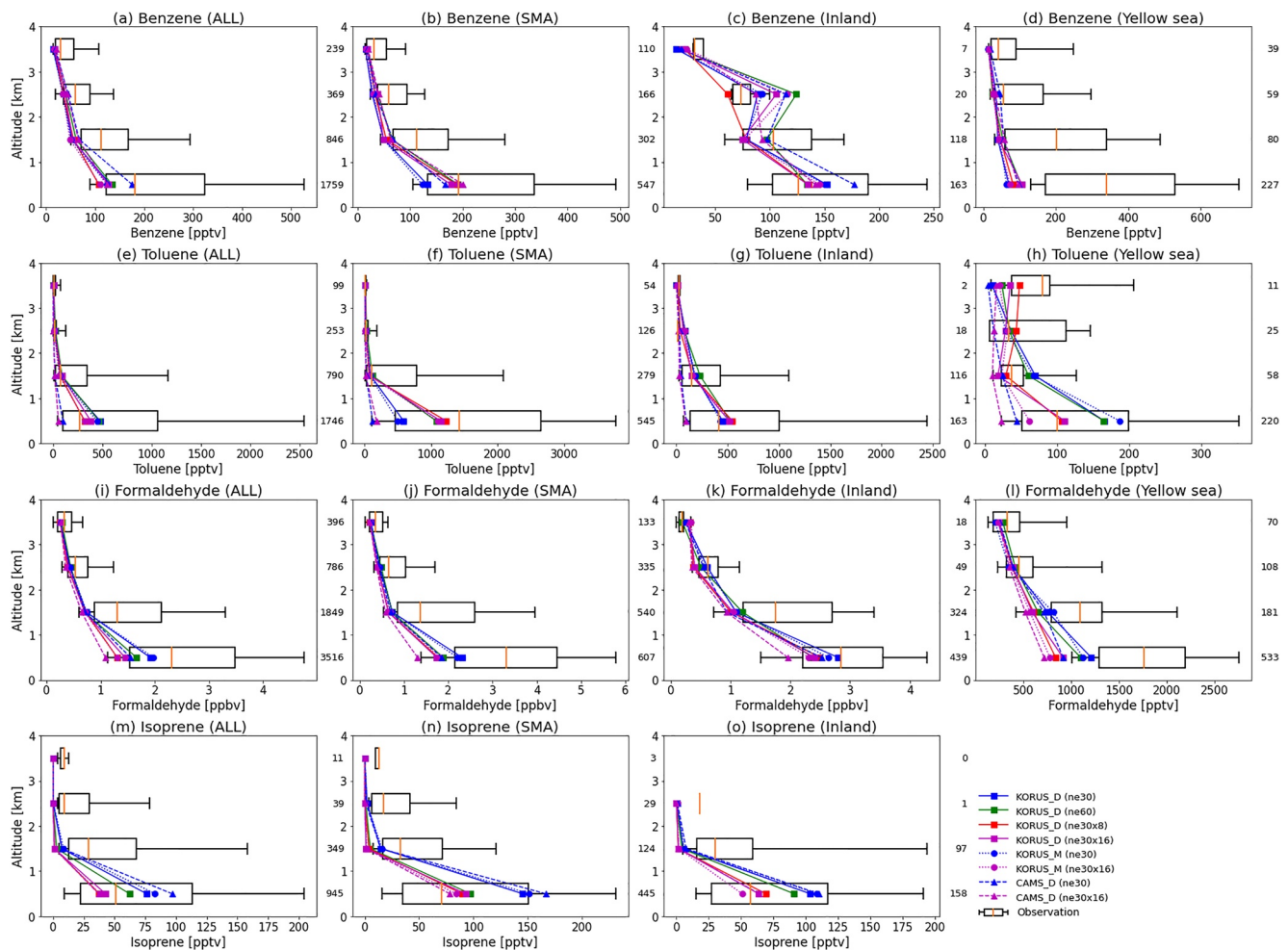
Figure 11. Vertical profiles of OH (a, b, c, d), and HO$_2$ (e, f, g, h) over the Korea-United States Air Quality (KORUS-AQ) flight tracks for four regions, the whole campaign ("ALL"), the Seoul Metropolitan Area ("SMA," 37.0°N–37.6°N, 126.6°E–127.7°E), Inland South Korea ("Inland," 35.0°N–37.0°N, 127.0°E–129.0°E), and the Yellow Sea (30.0°N–38.0°N, 123.0°E–125.0°E). The regions defined in this plot are shown in Figure S11 in Supporting Information S1. The model median values from the three simulations are plotted—KORUS_D (KORUSv5 with diurnal cycle applied to emissions; square, solid line), KORUS_M (KORUSv5 without diurnal cycle of emissions; circle, dotted line), and CAMS_D (CAMSv5.1 with diurnal cycle applied to emissions; triangle, dashed line), for ne30 (blue), ne60 (green), ne30x8 (red), and ne30x16 (purple) grid resolutions.

port (Wolfe et al., 2019), the use of high-resolution models over urban areas is crucial for accurately simulating the downwind transport of these species.

The differences between the models are more pronounced for highly reactive VOCs, such as toluene, compared to less reactive ones, such as benzene (Figure 12). For example, the ratio between ne30x16 and ne30 grid results at the lowest altitude bin is 1.34 for benzene and 1.95 for toluene over the SMA region. The underestimation of toluene using the CAMS-GLOB-ANTv5.1 emission inventory is significantly improved with the use of KORUSv5 inventory. The mean biases for CAMS_D simulations are −86% (ne30) and −77% (ne30x16), while those for KORUS_D simulations are −32% (ne30) and 12% (ne30x16). As demonstrated in Figure 12h over the Yellow Sea, it is essential for chemistry models to have up-to-date information and local statistics in order to accurately simulate not only local air quality but also long-range transport (Janssens-Maenhout et al., 2015).

The mixing ratios of isoprene are typically well-represented in regional refinement grids at altitudes below 1 km (Figure 12). This is likely due to the ability of the models to capture the spatial distribution of isoprene emissions, as isoprene is a highly reactive species (represented on the *x*-axis of Figure 6). However, the models substantially underestimate isoprene at altitudes above 1 km. As OH concentrations in models are generally comparable to the observations (Figure 11), and initial oxidation of isoprene is well established (Wennberg et al., 2018), there could be dynamics-related processes that are inadequately simulated in the model. This higher vertical gradient of isoprene

Figure 12. Vertical profiles of benzene (a, b, c, d), toluene (e, f, g, h), formaldehyde (i, j, k, l), and isoprene measured by whole air sampling (m, n, o) over the Korea-United States Air Quality (KORUS-AQ) flight tracks for four regions, the whole campaign ("ALL"), the Seoul Metropolitan Area ("SMA," 37.0°N–37.6°N, 126.6°E–127.7°E), Inland South Korea ("Inland," 35.0°N–37.0°N, 127.0°E–129.0°E), and the Yellow Sea (30.0°N–38.0°N, 123.0°E–125.0°E). Isoprene over the Yellow Sea is not shown due to insufficient data points above detection. The regions defined in this plot are shown in Figure S11 in Supporting Information S1. The model median values from the three simulations are plotted—KORUS_D (KORUSv5 with diurnal cycle applied to emissions; square, solid line), KORUS_M (KORUSv5 without diurnal cycle of emissions; circle, dotted line), and CAMS_D (CAMSv5.1 with diurnal cycle applied to emissions; triangle, dashed line), for ne30 (blue), ne60 (green), ne30x8 (red), and ne30x16 (purple) grid resolutions.

in models than in observations was also reported in the multi-model intercomparison study (Park et al., 2021). It is worth mentioning that the isoprene measurements used in this study were taken by WAS, which differs from the PTR-MS measurements used in previous KORUS-AQ modeling studies (Kwon et al., 2021; Park et al., 2021).

Isoprene measured by the PTR-MS (157 pptv; based on the average value calculated from R6 merge data when both WAS and PTR-MS measurements are available) is double the amount of isoprene measured by WAS (77 pptv) during KORUS-AQ. The measurement of isoprene by PTR-MS has interference from other hydrocarbons, particularly in areas with high anthropogenic VOCs like Seoul and Daesan (Figure S29a in Supporting Information S1). It has been shown that multiple other species can contribute to the m/z 69 signal in the PTR-MS, including pentanal, methyl butanal, and pentenol (de Gouw et al., 2003; Dunne et al., 2018). As shown in the scatterplot between PTR-MS and WAS colored by cyclopentane (Figure S29d in Supporting Information S1), PTR-MS isoprene is higher than WAS isoprene when anthropogenic influence is strong. Previous modeling studies that reported no significant bias against the measured isoprene by PTR-MS (e.g., Park et al., 2021) may have actually overestimated isoprene if the interference was corrected. Therefore, it is necessary to conduct further studies on the calculation and measurements of isoprene emissions in South Korea.
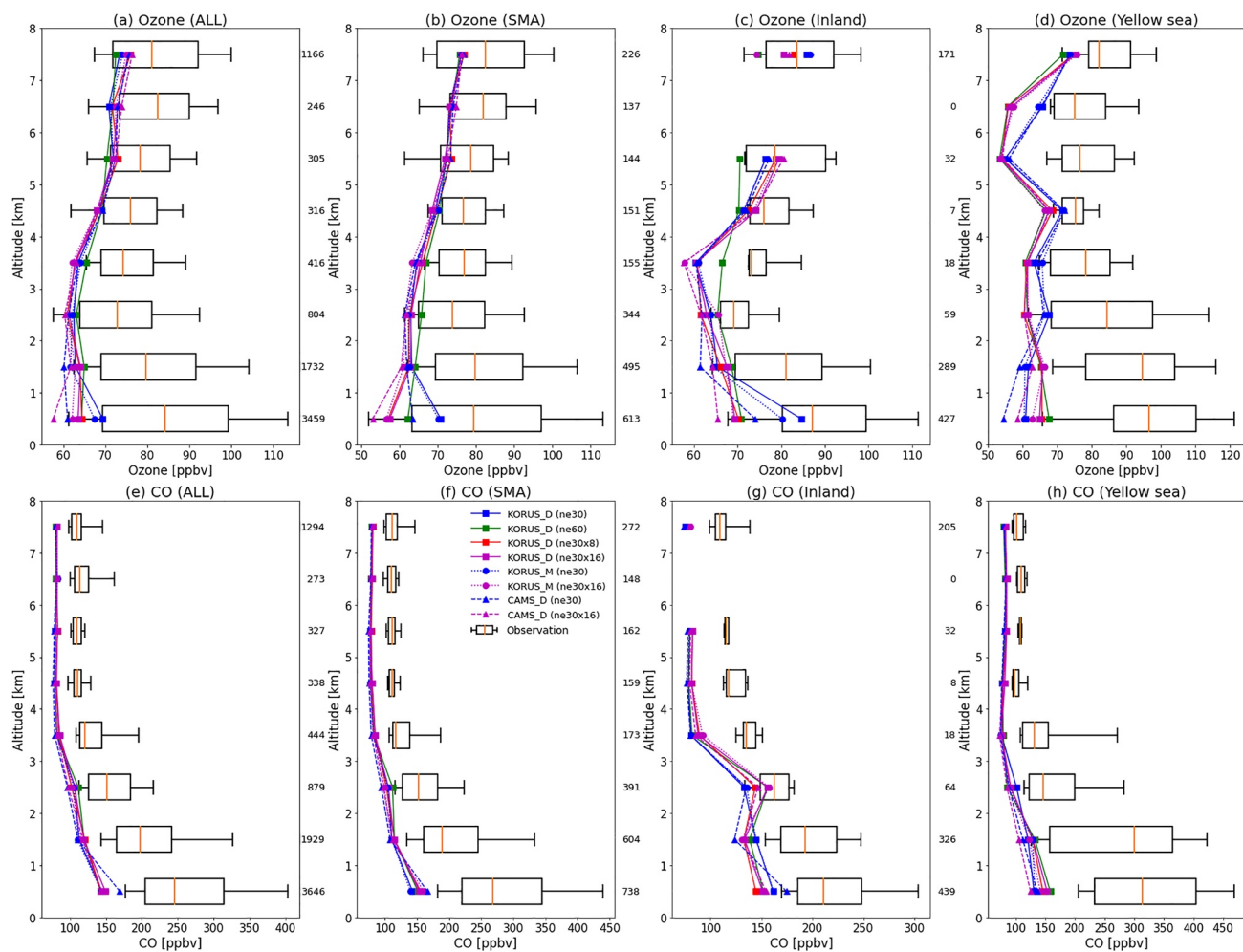
Figure 13. Vertical profiles of O$_3$ (a, b, c, d) and CO (e, f, g, h) over the Korea-United States Air Quality (KORUS-AQ) flight tracks for four regions, the whole campaign ("ALL"), Seoul Metropolitan Area ("SMA," 37.0°N–37.6°N, 126.6°E–127.7°E), Inland South Korea ("Inland," 35.0°N–37.0°N, 127.0°E–129.0°E), and the Yellow sea (30.0°N–38.0°N, 123.0°E–125.0°E). The regions defined in this plot are shown in Figure S11 in Supporting Information S1. The model median values from the three simulations are plotted—KORUS_D (KORUSv5 with diurnal cycle applied to emissions; square, solid line), KORUS_M (KORUSv5 without diurnal cycle of emissions; circle, dotted line), and CAMS_D (CAMSv5.1 with diurnal cycle applied to emissions; triangle, dashed line), for ne30 (blue), ne60 (green), ne30x8 (red), and ne30x16 (purple) grid resolutions.

Both ozone and CO are underestimated in the model (Figure 13), which is consistent with the findings of previous studies during KORUS-AQ (Gaubert et al., 2020; Oak et al., 2019; Park et al., 2021; Tang et al., 2018). As NO and NO$_2$ are generally well captured by the model (Figure 10) but formaldehyde is underestimated (mean biases are −25% and −34% for ne30 and ne30x16, respectively), the underestimation of ozone is likely due to missing VOCs and OVOCs in the model. According to Schroeder et al. (2020), the ozone production environment in the SMA is a VOC-limited regime. Oak et al. (2019) showed that enhancing the detailed aromatic chemistry leads to better simulated ozone due to increased NO to NO$_2$ conversion. Chemical mechanisms in atmospheric chemistry models, including MUSICAv0, have been simplified for alkanes such as butane and pentanes, which can also lead to lower performance of ozone simulations in high-resolution models due to missing chemical pathways such as converting NO to reservoir species and thus reducing the NO$_x$ titration effect. On the other hand, the use of KORUSv5 increases ozone in the lower troposphere, likely due to the overall increase in VOC emissions in the KORUSv5 inventory (Table 1), highlighting the importance of detailed local information.

The underestimation of CO in models is a persistent issue, not confined to KORUS-AQ but applying to other regions especially throughout the Northern Hemisphere (Emmons et al., 2020). Gaubert et al. (2020) investigated the CO underestimation in models during KORUS-AQ and suggested the cause to be an underestimation of anthropogenic CO sources in East Asia (up to 80% for northern China). The underestimation of CO is not
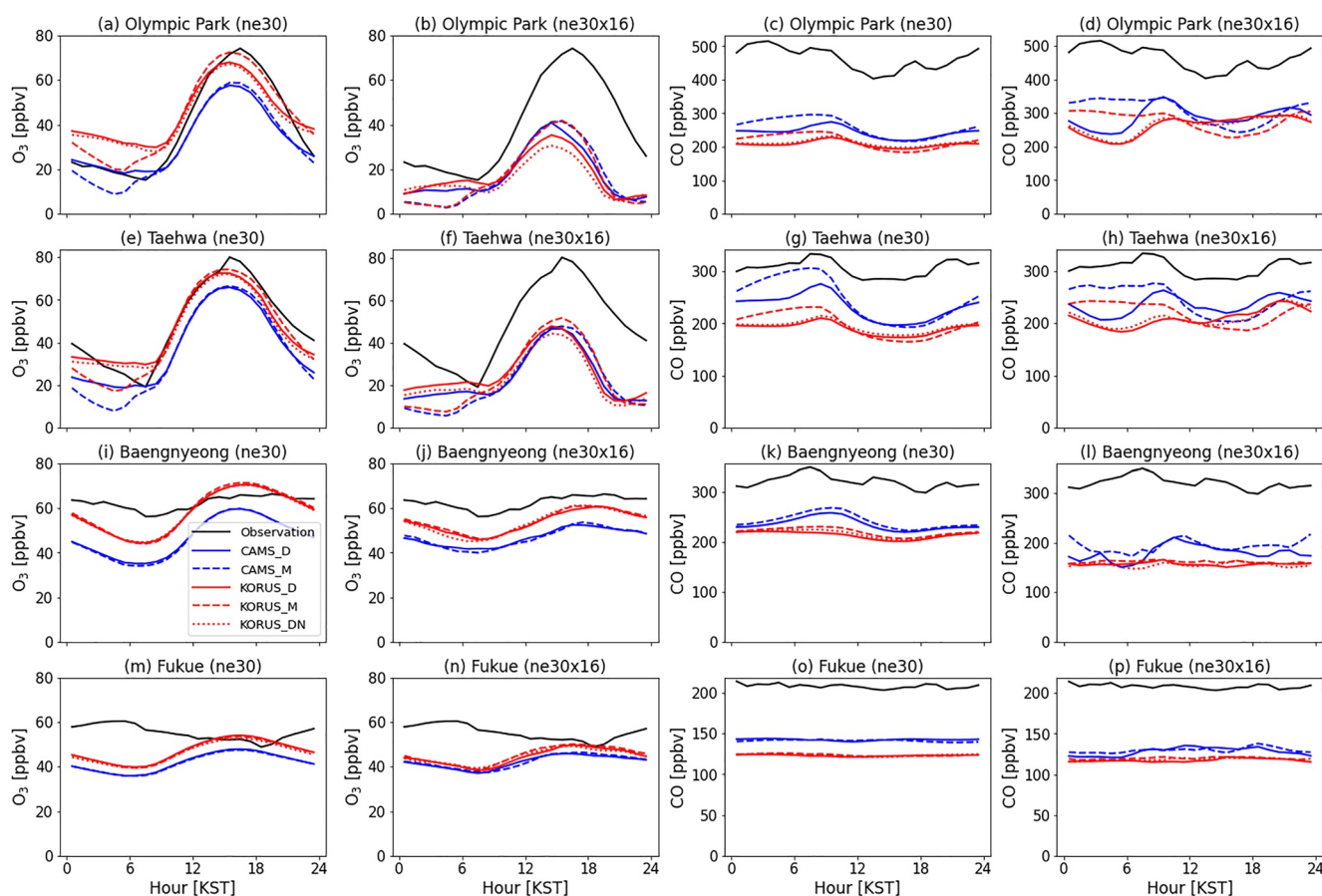
Figure 14. Model evaluation of average diurnal profiles of surface ozone (left two columns) and CO (right two columns) during the entire Korea-United States Air Quality campaign (1 May to 10 June 2016) at four observation sites (Olympic Park, 127.124°E, 37.522°N; Taehwa Forest, 127.311°E, 37.312°N; Baengnyeong Island, 124.617°E, 37.950°N; Fukue Island, 128.68°E, 32.75°N). Observations are shown in black, and model results are shown in blue (CAMS_D [solid] and CAMS_M [dashed]) and red (KORUS_D [solid], KORUS_M [dashed], and KORUS_DN [dotted]).

improved by changing the model resolution (−39% in ne30 to −38% in ne30x16), implying that other processes (e.g., emission, chemical mechanism) than grid resolution are important.

Overall, the model simulation results are improved for several species (OH, NO, NO$_2$, and toluene) with the use of high-resolution grids, but this is not always the case (e.g., PAN and formaldehyde). The evaluation of the model against aircraft measurements shows that the resolution of the grid does not have a significant impact on the simulation of major air pollutants like ozone and CO. Contrary to the results in Section 3.3, applying diurnal factors to emissions does not show an improvement in the model when compared to aircraft observations, because the diurnal variation has the greatest impact within the boundary layer at night, when there are no aircraft measurements available.

4.2. Surface Measurements

The comparison of the model simulations to the observed ozone and CO at four different locations—Olympic Park (urban), Taehwa Forest (urban downwind), Baengnyeong Island (rural), and Fukue Island (remote) is shown in Figure 14. Analogous to the aircraft comparison, the model generally underestimates surface ozone. However, contrary to the aircraft comparison, which shows all model simulations underestimate the observed ozone by more than 10 ppbv at the lowest level over the SMA (Figure 13b), some simulation cases reproduce the observed surface ozone with no significant bias. The global ne30 grid generally provides the best reproduction of observed ozone, and the effect of grid resolution becomes less important for rural/remote regions. The use of the KORUSv5 emission inventory with detailed local statistics generally improves the model performance. However, the best-performing model case (KORUS_M; red dashed line) may have achieved the right results for the wrong

reason, as this coarse model with no diurnal cycle shows the best results. The simulated ozone decreases as the model resolution increases from ne30 to ne30x8 (not shown) but ne30x8 and ne30x16 show similar levels of ozone, indicating convergence of the model results after reaching a specific resolution (ne30x8 in this case).

Carbon monoxide is again underestimated at the surface with the difference between model cases increasing (Figure 14). The differences between models over the SMA (or at Olympic Park) are ~20 ppbv for the aircraft comparison and ~100 ppbv for the surface comparison. The difference driven by the emission inventory is more noticeable at the surface even in remote regions (Fukue). Unlike ozone, the model using CAMS-GLOB-ANTv5.1 shows better evaluation results, due to its two times higher CO emissions over South Korea, highlighting the importance of emission inventory selection. This demonstrates that one emission inventory is not necessarily superior to another for all chemical species. In general, model results at the surface are more affected by grid resolution and emissions, than by the aircraft evaluation.

5. Conclusions

The recent advancements in global chemistry models have made it possible to simulate chemical species on unstructured grids with variable resolution. The new chemistry model framework MUSICA, which is being developed at NCAR in collaboration with the atmospheric chemistry community, offers the capability to conduct global simulations with regional refinement down to several kilometers. This study aimed to provide a comprehensive analysis of the impact of grid resolution and emission inventory on the simulation of various chemical species. Despite the significant changes in chemical species that occur due to grid resolution, there is limited information available to determine the optimal set-up for high-resolution simulations. The findings of this study can serve as the basis for next-generation models with variable resolution. Our main findings are as follows.

- For chemical concentrations at the surface level, the model results can vary up to 10 times due to grid resolution, depending on the species and location. The grid resolution is especially important for chemical species with these characteristics: (a) high spatial gradients in emission flux, (b) high reactivity (or short lifetime), and (c) dominated by primary emission sources. However, the model resolution also plays a significant role in the simulation of species with low reactivity or secondary species (e.g., surface ozone and formaldehyde). Additionally, variations in nighttime NO_3 concentrations due to changes in grid resolution can greatly affect the formation of organic nitrates resulting from the branching ratios of VOC oxidation.

- OH reactivities can change by up to a factor of three depending on the grid resolution over urban areas. The OH reactivities in mountainous areas show relatively similar levels across the different grid resolutions, however, the diurnal cycle and the proportion of different species contributing to OH reactivity vary. The high-resolution grid can be important for regions with small mountains such as South Korea, where cities are typically located within 50 km of the mountains.

- While isoprene emissions are consistently modeled across configurations and resolutions, the total LAI values differ substantially between SP and BGC simulations. Hence, the consistency found in this study cannot ensure equivalence in other regions or time periods. Since various factors are used to calculate biogenic emissions in MUSICAv0, future studies using the prognostic LAI will need to evaluate the land model variables first, especially if the results are heavily impacted by biogenic emissions.

- Although changes due to the two different emission inventories used here are generally less than changes due to grid resolutions, the emission inventory with detailed local information is important for predicting several chemical species (e.g., SO_2, toluene, ethane over South Korea). Imposing the diurnal cycle on monthly emissions is also essential for nighttime chemistry and chemical species with strong diurnal variations (e.g., ozone, NO_x, NO_3). NO_x speciation does not affect the simulation significantly even at a 7 km resolution.

- In terms of evaluating the model against aircraft measurements, simulations with high-resolution grids generally show better results, but not always. The concentrations of NO_x, OH, HNO_3, and toluene are better represented in high-resolution grid simulations, while PAN and formaldehyde are closer to observations in coarse-model grid simulations. There are no significant changes in the simulation of benzene, ozone, and CO. Surface CO is slightly improved in high-resolution simulations, particularly over urban areas, but the emission inventory has a more significant impact. Surface ozone is greatly underestimated in high-resolution grids due to the NO_x titration effect. The coarse model (ne30) with no diurnal cycle shows the best results in reproducing ozone, which is likely due to compensating errors.

- While there are substantial changes in simulated chemical concentrations between the ne30 and ne60 resolutions, and the ne60 and ne30x8 resolutions, the differences between the ne30x8 and ne30x16 resolutions are small. In terms of computational efficiency, the ne30x8 (∼14 km) resolution would be sufficient for simulating chemistry over South Korea or other regions where the distance between cities and mountains is greater than in South Korea. The computational costs required for the ne30, ne60, ne30x8, and ne30x16 resolutions (KORUS_D) are 11k, 72k, 117k, and 241k pe-hr year^{-1}, respectively, on the NCAR Cheyenne supercomputer.

The results of this study can be useful for chemical mechanism development, which is typically done using coarse grid global models (Bates et al., 2021; Schwantes et al., 2020). When evaluating the chemistry model against surface observations or aircraft measurements over urban areas, it is important to consider the grid resolution effects, as illustrated in Schwantes et al. (2022). However, the effects vary depending on the species, location, and time, and it is particularly important for reactive VOCs and nocturnal chemistry. The grid resolution is not a significant factor for CO, HNO_3, PAN, and formaldehyde. The high-resolution model performed poorly compared to the low-resolution model when evaluating ozone, highlighting the importance of utilizing high-resolution grids when incorporating new chemistry findings, conducting data assimilation, and developing parameterizations in urban areas in future studies.

This is the first case study that systematically showed the advantages and disadvantages of regional refinement grids in various aspects. While the use of regional refinement grids within a global model has the potential to benefit air quality modeling studies, further efforts are required to improve the accuracy of their predictions. For example, this study focuses only on gas-phase chemistry, not aerosol chemistry, and is limited to a specific region and season. For longer-term climate studies, the findings in this study may not be important in terms of the Earth's radiation budget, unless the high-resolution grid is applied to the whole globe. Further case studies with regional refinement techniques will be necessary to fully understand the systematic characteristics of chemistry simulations.

Data Availability Statement

Aircraft and surface measurements during the KORUS-AQ field campaign are available at the NASA data archive: https://www-air.larc.nasa.gov/missions/korus-aq/. MUSICAv0 is a configuration of CESM2.2, which is an open-source community model available from: https://github.com/ESCOMP/CESM. The code modifications for including diurnal cycle of anthropogenic emissions, grid information files, and simulation results are available at [https://doi.org/10.5281/zenodo.8044736]. CAMS-GLOB-ANTv5.1 emission inventory is available at ECCAD database (https://eccad.aeris-data.fr). The KORUSv5 emission inventory is available at http://aisl.konkuk.ac.kr/#/emission_data/korus-aq_emissions.

References

Atkinson, R., & Arey, J. (2003). Atmospheric degradation of volatile organic compounds. *Chemical Reviews*, *103*(12), 4605–4638. https://doi.org/10.1021/cr0206420

Bates, K. H., Jacob, D. J., Li, K., Ivatt, P. D., Evans, M. J., Yan, Y., & Lin, J. (2021). Development and evaluation of a new compact mechanism for aromatic oxidation in atmospheric models. *Atmospheric Chemistry and Physics*, *21*(24), 18351–18374. https://doi.org/10.5194/acp-21-18351-2021

Bian, H., Chin, M., Hauglustaine, D. A., Schulz, M., Myhre, G., Bauer, S. E., et al. (2017). Investigation of global particulate nitrate from the AeroCom phase III experiment. *Atmospheric Chemistry and Physics*, *17*(21), 12911–12940. https://doi.org/10.5194/acp-17-12911-2017

Bindle, L., Martin, R. V., Cooper, M. J., Lundgren, E. W., Eastham, S. D., Auer, B. M., et al. (2021). Grid-stretching capability for the GEOS-Chem 13.0.0 atmospheric chemistry model. *Geoscientific Model Development*, *14*(10), 5977–5997. https://doi.org/10.5194/gmd-14-5977-2021

Bogenschutz, P. A., Gettelman, A., Morrison, H., Larson, V. E., Craig, C., & Schanen, D. P. (2013). Higher-order turbulence closure and its impact on climate simulations in the Community Atmosphere Model. *Journal of Climate*, *26*(23), 9655–9676. https://doi.org/10.1175/jcli-d-13-00075.1

Brasseur, G. P., & Jacob, D. J. (2017). *Modeling of atmospheric chemistry*. Cambridge University Press.

Brasseur, G. P., Orlando, J. J., & Tyndall, G. (1999). *Atmospheric chemistry and global change*. Oxford University Press.

Brown, H., Liu, X., Feng, Y., Jiang, Y., Wu, M., Lu, Z., et al. (2018). Radiative effect and climate impacts of brown carbon with the Community Atmosphere Model (CAM5). *Atmospheric Chemistry and Physics*, *18*(24), 17745–17768. https://doi.org/10.5194/acp-18-17745-2018

Brown, S. S., & Stutz, J. (2012). Nighttime radical observations and chemistry. *Chemical Society Reviews*, *41*(19), 6405–6447. https://doi.org/10.1039/c2cs35181a

Brune, W. H., Miller, D. O., Thames, A. B., Brosius, A. L., Barletta, B., Blake, D. R., et al. (2022). Observations of atmospheric oxidation and ozone production in South Korea. *Atmospheric Environment*, *269*, 118854. https://doi.org/10.1016/j.atmosenv.2021.118854

Clifton, O. E., Paulot, F., Fiore, A. M., Horowitz, L. W., Correa, G., Baublitz, C. B., et al. (2020). Influence of dynamic ozone dry deposition on ozone pollution. *Journal of Geophysical Research D: Atmospheres*, *125*(8), e2020JD032398. https://doi.org/10.1029/2020jd032398

Crawford, J. H., Ahn, J.-Y., Al-Saadi, J., Chang, L., Emmons, L. K., Kim, J., et al. (2021). The Korea--United States Air Quality (KORUS-AQ) field study. *Elementa: Science of the Anthropocene*, *9*(1), 00163. https://doi.org/10.1525/elementa.2020.00163

Crippa, M., Guizzardi, D., Muntean, M., Schaaf, E., Dentener, F., van Aardenne, J. A., et al. (2018). Gridded emissions of air pollutants for the period 1970–2012 within EDGAR v4.3.2. *Earth System Science Data*, *10*(4), 1987–2013. https://doi.org/10.5194/essd-10-1987-2018

Crippa, M., Oreggioni, G., Guizzardi, D., Muntean, M., Schaaf, E., Lo Vullo, E., et al. (2019). *Fossil CO_2 and GHG emissions of all world countries: 2019 report*. Publications Office of the European Union.

Crippa, M., Solazzo, E., Huang, G., Guizzardi, D., Koffi, E., Muntean, M., et al. (2020). High resolution temporal profiles in the emissions database for global atmospheric research. *Scientific Data*, *7*(1), 121. https://doi.org/10.1038/s41597-020-0462-2

Crounse, J. D., McKinney, K. A., Kwan, A. J., & Wennberg, P. O. (2006). Measurement of gas-phase hydroperoxides by chemical ionization mass spectrometry. *Analytical Chemistry*, *78*(19), 6726–6732. https://doi.org/10.1021/ac0604235

Darmenov, A., & da Silva, A. (2015). The Quick fire emissions dataset (QFED): Documentation of versions 2.1, 2.2 and 2.4. Volume 38; Technical Report Series on Global Modeling and Data Assimilation. NASA Global Modeling and Assimilation Office. [online]. Retrieved from https://www.semanticscholar.org/paper/f18b64dce3bc0f3384d0d8377b409597c5c665cb

de Gouw, J. A., Goldan, P. D., Warneke, C., Kuster, W. C., Roberts, J. M., Marchewka, M., et al. (2003). Validation of proton transfer reaction-mass spectrometry (PTR-MS) measurements of gas-phase organic compounds in the atmosphere during the New England Air Quality Study (NEAQS) in 2002. *Journal of Geophysical Research*, *108*(D21), 4682. https://doi.org/10.1029/2003jd003863

Diehl, T., Heil, A., Chin, M., Pan, X., Streets, D., Schultz, M., & Kinne, S. (2012). Anthropogenic, biomass burning, and volcanic emissions of black carbon, organic carbon, and SO_2 from 1980 to 2010 for hindcast model experiments. *Atmospheric Chemistry and Physics Discussions*, *12*, 24895–24954.

Dunne, E., Galbally, I. E., Cheng, M., Selleck, P., Molloy, S. B., & Lawson, S. J. (2018). Comparison of VOC measurements made by PTR-MS, adsorbent tubes–GC-FID-MS and DNPH derivatization–HPLC during the Sydney Particle Study, 2012: A contribution to the assessment of uncertainty in routine atmospheric VOC measurements. *Atmospheric Measurement Techniques*, *11*(1), 141–159. https://doi.org/10.5194/amt-11-141-2018

Eastham, S. D., Long, M. S., Keller, C. A., Lundgren, E., Yantosca, R. M., Zhuang, J., et al. (2018). GEOS-Chem high performance (GCHP v11-02c): A next-generation implementation of the GEOS-Chem chemical transport model for massively parallel applications. *Geoscientific Model Development*, *11*(7), 2941–2953. https://doi.org/10.5194/gmd-11-2941-2018

Elguindi, N., Granier, C., Stavrakou, T., Darras, S., Bauwens, M., Cao, H., et al. (2020). Intercomparison of magnitudes and trends in anthropogenic surface emissions from bottom-up inventories, top-down estimates, and emission scenarios. *Earth's Future*, *8*(8), e2020EF001520. https://doi.org/10.1029/2020EF001520

Emmons, L. K., Schwantes, R. H., Orlando, J. J., Tyndall, G., Kinnison, D., Lamarque, J., et al. (2020). The chemistry mechanism in the Community Earth System Model Version 2 (CESM2). *Journal of Advances in Modeling Earth Systems*, *12*(4), e2019MS001882. https://doi.org/10.1029/2019ms001882

Fahey, D. W., Gao, R. S., Carslaw, K. S., Kettleborough, J., Popp, P. J., Northway, M. J., et al. (2001). The detection of large HNO_3-containing particles in the winter Arctic stratosphere. *Science*, *291*(5506), 1026–1031. https://doi.org/10.1126/science.1057265

Fairlie, T. D., Liu, H., Vernier, J., Campuzano-Jost, P., Jimenez, J. L., Jo, D. S., et al. (2020). Estimates of regional source contributions to the Asian tropopause aerosol layer using a chemical transport model. *Journal of Geophysical Research D: Atmospheres*, *125*(4), 18607. https://doi.org/10.1029/2019jd031506

Fried, A., Walega, J., Weibring, P., Richter, D., Simpson, I. J., Blake, D. R., et al. (2020). Airborne formaldehyde and volatile organic compound measurements over the Daesan petrochemical complex on Korea's northwest coast during the Korea-United States Air Quality study. *Elementa*, *8*(1), 121. https://doi.org/10.1525/elementa.2020.121

Gao, M., Han, Z., Liu, Z., Li, M., Xin, J., Tao, Z., et al. (2018). Air quality and climate change, Topic 3 of the model inter-comparison study for Asia phase III (MICS-Asia III) – Part 1: Overview and model evaluation. *Atmospheric Chemistry and Physics*, *18*(7), 4859–4884. https://doi.org/10.5194/acp-18-4859-2018

Gaubert, B., Emmons, L. K., Raeder, K., Tilmes, S., Miyazaki, K., Arellano, A. F., Jr., et al. (2020). Correcting model biases of CO in East Asia: Impact on oxidant distributions during KORUS-AQ. *Atmospheric Chemistry and Physics*, *20*(23), 14617–14647. https://doi.org/10.5194/acp-20-14617-2020

Gelaro, R., McCarty, W., Suárez, M. J., Todling, R., Molod, A., Takacs, L., et al. (2017). The modern-era retrospective analysis for research and applications, version 2 (MERRA-2). *Journal of Climate*, *30*(13), 5419–5454. https://doi.org/10.1175/jcli-d-16-0758.1

Gettelman, A., & Morrison, H. (2015). Advanced two-moment bulk microphysics for global models. Part I: Off-line tests and comparison with other schemes. *Journal of Climate*, *28*(3), 1268–1287. https://doi.org/10.1175/jcli-d-14-00102.1

Gliß, J., Mortier, A., Schulz, M., Andrews, E., Balkanski, Y., Bauer, S. E., et al. (2021). AeroCom phase III multi-model evaluation of the aerosol life cycle and optical properties using ground- and space-based remote sensing as well as surface in situ observations. *Atmospheric Chemistry and Physics*, *21*(1), 87–128. https://doi.org/10.5194/acp-21-87-2021

Golaz, J.-C., Larson, V. E., & Cotton, W. R. (2002). A PDF-based model for boundary layer clouds. Part I: Method and model description. *Journal of the Atmospheric Sciences*, *59*(24), 3540–3551. https://doi.org/10.1175/1520-0469(2002)059<3540:apbmfb>2.0.co;2

Goto, D., Sato, Y., Yashiro, H., Suzuki, K., Oikawa, E., Kudo, R., et al. (2020). Global aerosol simulations using NICAM.16 on a 14 km grid spacing for a climate study: Improved and remaining issues relative to a lower-resolution model. *Geoscientific Model Development*, *13*(8), 3731–3768. https://doi.org/10.5194/gmd-13-3731-2020

Granier, C., Darras, S., Denier van der Gon, H., Doubalova, J., Elguindi, N., Galle, B., et al. (2019). The copernicus atmosphere monitoring service global and regional emissions (April 2019 version). https://doi.org/10.24380/D0BN-KX16

Granier, C., Lamarque, J. F., Mieville, A., Muller, J. F., Olivier, J., Orlando, J., et al. (2005). POET, a database of surface emissions of ozone precursors. GEIA-ACCENT documentation [online]. Retrieved from http://www.pole-ether.fr/eccad

Guenther, A., Karl, T., Harley, P., Wiedinmyer, C., Palmer, P. I., & Geron, C. (2006). Estimates of global terrestrial isoprene emissions using MEGAN (model of emissions of gases and aerosols from nature). *Atmospheric Chemistry and Physics*, *6*(11), 3181–3210. https://doi.org/10.5194/acp-6-3181-2006

Guenther, A. B., Jiang, X., Heald, C. L., Sakulyanontvittaya, T., Duhl, T., Emmons, L. K., & Wang, X. (2012). The model of emissions of gases and aerosols from nature version 2.1 (MEGAN2.1): An extended and updated framework for modeling biogenic emissions. *Geoscientific Model Development*, *5*(6), 1471–1492. https://doi.org/10.5194/gmd-5-1471-2012

Herrington, A. R., & Reed, K. A. (2020). On resolution sensitivity in the Community Atmosphere Model. *Quarterly Journal of the Royal Meteorological Society*, *146*(733), 3789–3807. https://doi.org/10.1002/qj.3873

Hoesly, R. M., Smith, S. J., Feng, L., Klimont, Z., Janssens-Maenhout, G., Pitkanen, T., et al. (2018). Historical (1750–2014) anthropogenic emissions of reactive gases and aerosols from the Community Emissions Data System (CEDS). *Geoscientific Model Development*, *11*(1), 369–408. https://doi.org/10.5194/gmd-11-369-2018

Horowitz, L. W., Naik, V., Paulot, F., Ginoux, P. A., Dunne, J. P., Mao, J., et al. (2020). The GFDL global atmospheric chemistry-climate model AM4.1: Model description and simulation characteristics. *Journal of Advances in Modeling Earth Systems*, *12*(10), e2019MS002032. https://doi.org/10.1029/2019ms002032

Hrdina, A., Murphy, J. G., Hallar, A. G., Lin, J. C., Moravek, A., Bares, R., et al. (2021). The role of coarse aerosol particles as a sink of HNO_3 in wintertime pollution events in the Salt Lake Valley. *Atmospheric Chemistry and Physics*, *21*(10), 8111–8126. https://doi.org/10.5194/acp-21-8111-2021

Hu, L., Keller, C. A., Long, M. S., Sherwen, T., Auer, B., Da Silva, A., et al. (2018). Global simulation of tropospheric chemistry at 12.5 km resolution: Performance and evaluation of the GEOS-Chem chemical module (v10-1) within the NASA GEOS Earth system model (GEOS-5 ESM). *Geoscientific Model Development*, *11*(11), 4603–4620. https://doi.org/10.5194/gmd-11-4603-2018

Huang, G., Brook, R., Crippa, M., Janssens-Maenhout, G., Schieberle, C., Dore, C., et al. (2017). Speciation of anthropogenic emissions of non-methane volatile organic compounds: A global gridded data set for 1970–2012. *Atmospheric Chemistry and Physics*, *17*(12), 7683–7701. https://doi.org/10.5194/acp-17-7683-2017

Iacono, M. J., Delamere, J. S., Mlawer, E. J., Shephard, M. W., Clough, S. A., & Collins, W. D. (2008). Radiative forcing by long-lived greenhouse gases: Calculations with the AER radiative transfer models. *Journal of Geophysical Research*, *113*(D13), 233. https://doi.org/10.1029/2008jd009944

Janssens-Maenhout, G., Crippa, M., Guizzardi, D., Dentener, F., Muntean, M., Pouliot, G., et al. (2015). HTAP_v2. 2: A mosaic of regional and global emission grid maps for 2008 and 2010 to study hemispheric transport of air pollution. *Atmospheric Chemistry and Physics*, *15*(19), 11411–11432. https://doi.org/10.5194/acp-15-11411-2015

Jo, D. S., Hodzic, A., Emmons, L. K., Tilmes, S., Schwantes, R. H., Mills, M. J., et al. (2021). Future changes in isoprene-epoxydiol-derived secondary organic aerosol (IEPOX SOA) under the Shared Socioeconomic Pathways: The importance of physicochemical dependency. *Atmospheric Chemistry and Physics*, *21*(5), 3395–3425. https://doi.org/10.5194/acp-21-3395-2021

Jo, D. S., Park, R. J., Kim, M. J., & Spracklen, D. V. (2013). Effects of chemical aging on global secondary organic aerosol using the volatility basis set approach. *Atmospheric Environment*, *81*, 230–244. https://doi.org/10.1016/j.atmosenv.2013.08.055

Jo, D. S., Park, R. J., Lee, S., Kim, S.-W., & Zhang, X. (2016). A global simulation of brown carbon: Implications for photochemistry and direct radiative effect. *Atmospheric Chemistry and Physics*, *16*(5), 3413–3432. https://doi.org/10.5194/acp-16-3413-2016

Jones, P. W. (1999). First- and second-order conservative remapping schemes for grids in spherical coordinates. *Monthly Weather Review*, *127*(9), 2204–2210. https://doi.org/10.1175/1520-0493(1999)127<2204:fasocr>2.0.co;2

Keller, C. A., Long, M. S., Yantosca, R. M., Da Silva, A. M., Pawson, S., & Jacob, D. J. (2014). HEMCO v1.0: A versatile, ESMF-compliant component for calculating emissions in atmospheric models. *Geoscientific Model Development*, *7*(4), 1409–1417. https://doi.org/10.5194/gmd-7-1409-2014

Kim, P. S., Jacob, D. J., Fisher, J. A., Travis, K., Yu, K., Zhu, L., et al. (2015). Sources, seasonality, and trends of southeast US aerosol: An integrated analysis of surface, aircraft, and satellite observations with the GEOS-Chem chemical transport model. *Atmospheric Chemistry and Physics*, *15*(18), 10411–10433. https://doi.org/10.5194/acp-15-10411-2015

Krol, M., Houweling, S., Bregman, B., van den Broek, M., Segers, A., van Velthoven, P., et al. (2005). The two-way nested global chemistry-transport zoom model TM5: Algorithm and applications. *Atmospheric Chemistry and Physics*, *5*(2), 417–432. https://doi.org/10.5194/acp-5-417-2005

Kurokawa, J., & Ohara, T. (2020). Long-term historical trends in air pollutant emissions in Asia: Regional Emission inventory in ASia (REAS) version 3. *Atmospheric Chemistry and Physics*, *20*(21), 12761–12793. https://doi.org/10.5194/acp-20-12761-2020

Kwon, H.-A., Park, R. J., Oak, Y. J., Nowlan, C. R., Janz, S. J., Kowalewski, M. G., et al. (2021). Top-down estimates of anthropogenic VOC emissions in South Korea using formaldehyde vertical column densities from aircraft during the KORUS-AQ campaign. *Elementa*, *9*(1), 00109. https://doi.org/10.1525/elementa.2021.00109

Lauritzen, P. H., Jablonowski, C., Taylor, M. A., & Nair, R. D. (2010). Rotated versions of the Jablonowski steady-state and baroclinic wave test cases: A dynamical core intercomparison. *Journal of Advances in Modeling Earth Systems*, *2*(4), 34. https://doi.org/10.3894/james.2010.2.15

Lauritzen, P. H., Nair, R. D., Herrington, A. R., Callaghan, P., Goldhaber, S., Dennis, J. M., et al. (2018). NCAR release of CAM-SE in CESM2.0: A reformulation of the spectral element dynamical core in dry-mass vertical coordinates with comprehensive treatment of condensates and energy. *Journal of Advances in Modeling Earth Systems*, *10*(7), 1537–1570. https://doi.org/10.1029/2017ms001257

Lawrence, D. M., Fisher, R. A., Koven, C. D., Oleson, K. W., Swenson, S. C., Bonan, G., et al. (2019). The Community Land Model Version 5: Description of new features, benchmarking, and impact of forcing uncertainty. *Journal of Advances in Modeling Earth Systems*, *11*(12), 4245–4287. https://doi.org/10.1029/2018ms001583

Li, B., Ho, S. S. H., Li, X., Guo, L., Chen, A., Hu, L., et al. (2021). A comprehensive review on anthropogenic volatile organic compounds (VOCs) emission estimates in China: Comparison and outlook. *Environment International*, *156*, 106710. https://doi.org/10.1016/j.envint.2021.106710

Lin, H., Jacob, D. J., Lundgren, E. W., Sulprizio, M. P., Keller, C. A., Fritz, T. M., et al. (2021). Harmonized emissions component (HEMCO) 3.0 as a versatile emissions component for atmospheric models: Application in the GEOS-Chem, NASA GEOS, WRF-GC, CESM2, NOAA GEFS-aerosol, and NOAA UFS models. *Geoscientific Model Development*, *14*(9), 5487–5506. https://doi.org/10.5194/gmd-14-5487-2021

Liu, X., Ma, P.-L., Wang, H., Tilmes, S., Singh, B., Easter, R. C., et al. (2016). Description and evaluation of a new four-mode version of the modal aerosol module (MAM4) within version 5.3 of the Community Atmosphere Model. *Geoscientific Model Development*, *9*(2), 505–522. https://doi.org/10.5194/gmd-9-505-2016

Marais, E. A., & Wiedinmyer, C. (2016). Air quality impact of diffuse and inefficient combustion emissions in Africa (DICE-Africa). *Environmental Science & Technology*, *50*(19), 10739–10745. https://doi.org/10.1021/acs.est.6b02602

McDuffie, E. E., Smith, S. J., O'Rourke, P., Tibrewal, K., Venkataraman, C., Marais, E. A., et al. (2020). A global anthropogenic emission inventory of atmospheric pollutants from sector- and fuel-specific sources (1970–2017): An application of the Community Emissions Data System (CEDS). *Earth System Science Data*, *12*(4), 3413–3442. https://doi.org/10.5194/essd-12-3413-2020

Meidan, D., Holloway, J. S., Edwards, P. M., Dubé, W. P., Middlebrook, A. M., Liao, J., et al. (2019). Role of Criegee intermediates in secondary sulfate aerosol formation in nocturnal power plant plumes in the Southeast US. *ACS Earth and Space Chemistry*, *3*(5), 748–759. https://doi.org/10.1021/acsearthspacechem.8b00215

Menut, L., Bessagnet, B., Colette, A., & Khvorostyanov, D. (2013). On the impact of the vertical resolution on chemistry-transport modelling. *Atmospheric Environment*, *67*, 370–384. https://doi.org/10.1016/j.atmosenv.2012.11.026

Mills, M. J., Schmidt, A., Easter, R., Solomon, S., Kinnison, D. E., Ghan, S. J., et al. (2016). Global volcanic aerosol properties derived from emissions, 1990–2014, using CESM1(WACCM). *Journal of Geophysical Research: Atmospheres*, *121*(5), 2332–2348. https://doi.org/10.1002/2015jd024290

Müller, M., Mikoviny, T., Feil, S., Haidacher, S., Hanel, G., Hartungen, E., et al. (2014). A compact PTR-ToF-MS instrument for airborne measurements of volatile organic compounds at high spatiotemporal resolution. *Atmospheric Measurement Techniques*, *7*(11), 3763–3772. https://doi.org/10.5194/amt-7-3763-2014

Neely, R. R., III, & Schmidt, A. (2016). *VolcanEESM: Global volcanic sulphur dioxide (SO₂) emissions database from 1850 to present*. Centre for Environmental Data Analysis. https://doi.org/10.5285/76ebdc0b-0eed-4f70-b89e-55e606bcd568

Nicely, J. M., Salawitch, R. J., Canty, T., Anderson, D. C., Arnold, S. R., Chipperfield, M. P., et al. (2017). Quantifying the causes of differences in tropospheric OH within global models. *Journal of Geophysical Research D: Atmospheres*, *122*(3), 1983–2007. https://doi.org/10.1002/2016jd026239

Oak, Y. J., Park, R. J., Schroeder, J. R., Crawford, J. H., Blake, D. R., Weinheimer, A. J., et al. (2019). Evaluation of simulated O₃ production efficiency during the KORUS-AQ campaign: Implications for anthropogenic NOx emissions in Korea. *Elementa: Science of the Anthropocene*, *7*(1), 56. https://doi.org/10.1525/elementa.394

Orlando, J. J., Tyndall, G. S., Moortgat, G. K., & Calvert, J. G. (1993). Quantum yields for nitrate radical photolysis between 570 and 635 nm. *Journal of Physical Chemistry A*, *97*(42), 10996–11000. https://doi.org/10.1021/j100144a017

Otto, S. A. (2019). How to normalize the RMSE. [online]. Retrieved from https://www.marinedatascience.co/blog/2019/01/07/normalizing-the-rmse/

Paolella, D. A., Tessum, C. W., Adams, P. J., Apte, J. S., Chambliss, S., Hill, J., et al. (2018). Effect of model spatial resolution on estimates of fine particulate matter exposure and exposure disparities in the United States. *Environmental Science & Technology Letters*, *5*(7), 436–441. https://doi.org/10.1021/acs.estlett.8b00279

Park, R. J., Oak, Y. J., Emmons, L. K., Kim, C.-H., Pfister, G. G., Carmichael, G. R., et al. (2021). Multi-model intercomparisons of air quality simulations for the KORUS-AQ campaign. *Elementa: Science of the Anthropocene*, *9*(1), 00139. https://doi.org/10.1525/elementa.2021.00139

Park, R. J., Pickering, K. E., Allen, D. J., Stenchikov, G. L., & Fox-Rabinovitz, M. S. (2004). Global simulation of tropospheric ozone using the University of Maryland Chemical Transport Model (UMD-CTM): 1. Model description and evaluation. *Journal of Geophysical Research D: Atmospheres*, *109*(D9), D09301. https://doi.org/10.1029/2003JD004266

Paulot, F., Crounse, J. D., Kjaergaard, H. G., Kürten, A., St Clair, J. M., Seinfeld, J. H., & Wennberg, P. O. (2009). Unexpected epoxide formation in the gas-phase photooxidation of isoprene. *Science*, *325*(5941), 730–733. https://doi.org/10.1126/science.1172910

Pfister, G. G., Eastham, S. D., Arellano, A. F., Aumont, B., Barsanti, K. C., Barth, M. C., et al. (2020). The multi-scale infrastructure for chemistry and aerosols (MUSICA). *Bulletin of the American Meteorological Society*, *101*(10), E1743–E1760. https://doi.org/10.1175/bams-d-19-0331.1

Price, C., Penner, J., & Prather, M. (1997). NOx from lightning: 1. Global distribution based on lightning physics. *Journal of Geophysical Research*, *102*(D5), 5929–5941. https://doi.org/10.1029/96jd03504

Punger, E. M., & West, J. J. (2013). The effect of grid resolution on estimates of the burden of ozone and fine particulate matter on premature mortality in the USA. *Air Quality, Atmosphere & Health*, *6*(3), 563–573. https://doi.org/10.1007/s11869-013-0197-8

Pye, H. O. T., Chan, A. W. H., Barkley, M. P., & Seinfeld, J. H. (2010). Global modeling of organic aerosol: The importance of reactive nitrogen (NOₓ and NO₃). *Atmospheric Chemistry and Physics*, *10*(22), 11261–11276. https://doi.org/10.5194/acp-10-11261-2010

Richter, D., Weibring, P., Walega, J. G., Fried, A., Spuler, S. M., & Taubman, M. S. (2015). Compact highly sensitive multi-species airborne mid-IR spectrometer. *Applied Physics B*, *119*(1), 119–131. https://doi.org/10.1007/s00340-015-6038-8

Sachse, G. W., Collins, J. E., Jr., Hill, G. F., Wade, L. O., Burney, L. G., & Ritter, J. A. (1991). Airborne tunable diode laser sensor for high-precision concentration and flux measurements of carbon monoxide and methane. In *Measurement of atmospheric gases* (Vol. 1433, pp. 157–166). SPIE.

Schaap, M., Cuvelier, C., Hendriks, C., Bessagnet, B., Baldasano, J. M., Colette, A., et al. (2015). Performance of European chemistry transport models as function of horizontal resolution. *Atmospheric Environment*, *112*, 90–105. https://doi.org/10.1016/j.atmosenv.2015.04.003

Schroeder, J. R., Crawford, J. H., Ahn, J.-Y., Chang, L., Fried, A., Walega, J., et al. (2020). Observation-based modeling of ozone chemistry in the Seoul metropolitan area during the Korea-United States Air Quality Study (KORUS-AQ). *Elementa*, *8*(1), 3. https://doi.org/10.1525/elementa.400

Schwantes, R. H., Emmons, L. K., Orlando, J. J., Barth, M. C., Tyndall, G. S., Hall, S. R., et al. (2020). Comprehensive isoprene and terpene gas-phase chemistry improves simulated surface ozone in the southeastern US. *Atmospheric Chemistry and Physics*, *20*(6), 3739–3776. https://doi.org/10.5194/acp-20-3739-2020

Schwantes, R. H., Lacey, F. G., Tilmes, S., Emmons, L. K., Lauritzen, P. H., Walters, S., et al. (2022). Evaluating the impact of chemical complexity and horizontal resolution on tropospheric ozone over the conterminous US with a global variable resolution chemistry model. *Journal of Advances in Modeling Earth Systems*, *14*(6), e2021MS002889. https://doi.org/10.1029/2021ms002889

Schwantes, R. H., Teng, A. P., Nguyen, T. B., Coggon, M. M., Crounse, J. D., St Clair, J. M., et al. (2015). Isoprene NO₃ oxidation products from the RO₂ + HO₂ pathway. *Journal of Physical Chemistry A*, *119*(40), 10158–10171. https://doi.org/10.1021/acs.jpca.5b06355

Simpson, I. J., Blake, D. R., Blake, N. J., Meinardi, S., Barletta, B., Hughes, S. C., et al. (2020). Characterization, sources and reactivity of volatile organic compounds (VOCs) in Seoul and surrounding regions during KORUS-AQ. *Elementa: Science of the Anthropocene*, *8*(1), 37. https://doi.org/10.1525/elementa.434

Slusher, D. L., Huey, L. G., Tanner, D. J., Flocke, F. M., & Roberts, J. M. (2004). A thermal dissociation–chemical ionization mass spectrometry (TD-CIMS) technique for the simultaneous detection of peroxyacyl nitrates and dinitrogen pentoxide. *Journal of Geophysical Research D: Atmospheres*, *109*(D19), D19315. https://doi.org/10.1029/2004JD004670

Stone, D., Whalley, L. K., & Heard, D. E. (2012). Tropospheric OH and HO₂ radicals: Field measurements and model comparisons. *Chemical Society Reviews*, *41*(19), 6348–6404. https://doi.org/10.1039/c2cs35140d

Tang, W., Arellano, A. F., DiGangi, J. P., Choi, Y., Diskin, G. S., Agustí-Panareda, A., et al. (2018). Evaluating high-resolution forecasts of atmospheric CO and CO₂ from a global prediction system during KORUS-AQ field campaign. *Atmospheric Chemistry and Physics*, *18*(15), 11007–11030. https://doi.org/10.5194/acp-18-11007-2018

Tang, W., Pfister, G. G., Kumar, R., Barth, M., Edwards, D. P., Emmons, L. K., & Tilmes, S. (2023). Capturing high-resolution air pollution features using the multi-scale infrastructure for chemistry and aerosols version 0 (MUSICAv0) global modeling system. *Journal of Geophysical Research: Atmospheres*, *128*(7), e2022JD038345. https://doi.org/10.1029/2022jd038345

Tost, H., Jöckel, P., & Lelieveld, J. (2007). Lightning and convection parameterisations – Uncertainties in global modelling. *Atmospheric Chemistry and Physics*, *7*(17), 4553–4568. https://doi.org/10.5194/acp-7-4553-2007

Tsigaridis, K., Daskalakis, N., Kanakidou, M., Adams, P. J., Artaxo, P., Bahadur, R., et al. (2014). The AeroCom evaluation and intercomparison of organic aerosol in global models. *Atmospheric Chemistry and Physics*, *14*(19), 10845–10895. https://doi.org/10.5194/acp-14-10845-2014

Veres, P. R., Neuman, J. A., Bertram, T. H., Assaf, E., Wolfe, G. M., Williamson, C. J., et al. (2020). Global airborne sampling reveals a previously unobserved dimethyl sulfide oxidation mechanism in the marine atmosphere. *Proceedings of the National Academy of Sciences of the United States of America*, *117*(9), 4505–4510. https://doi.org/10.1073/pnas.1919344117

Wang, S., Coggon, M. M., Gkatzelis, G. I., Warneke, C., Bourgeois, I., Ryerson, T., et al. (2021). Chemical tomography in a fresh wildland fire plume: A large eddy simulation (LES) study. *Journal of Geophysical Research: Atmospheres*, *126*(18), e2021JD035203. https://doi.org/10.1029/2021jd035203

Wang, Y. X., McElroy, M. B., Jacob, D. J., & Yantosca, R. M. (2004). A nested grid formulation for chemical transport over Asia: Applications to CO. *Journal of Geophysical Research*, *109*(D22), D22307. https://doi.org/10.1029/2004jd005237

Wängberg, I., Etzkorn, T., Barnes, I., Platt, U., & Becker, K. H. (1997). Absolute determination of the temperature behavior of the $NO_2 + NO_3 +(M) \leftrightarrow N_2O_5 + (M)$ equilibrium. *Journal of Physical Chemistry A*, *101*(50), 9694–9698. https://doi.org/10.1021/jp972203o

Weinheimer, A. J., Walega, J. G., Ridley, B. A., Gary, B. L., Blake, D. R., Blake, N. J., et al. (1994). Meridional distributions of NO_x, NO_y, and other species in the lower stratosphere and upper troposphere during AASE II. *Geophysical Research Letters*, *21*(23), 2583–2586. https://doi.org/10.1029/94gl01897

Wennberg, P. O., Bates, K. H., Crounse, J. D., Dodson, L. G., McVay, R. C., Mertens, L. A., et al. (2018). Gas-phase reactions of isoprene and its major oxidation products. *Chemical Reviews*, *118*(7), 3337–3390. https://doi.org/10.1021/acs.chemrev.7b00439

Wiedinmyer, C., Akagi, S. K., Yokelson, R. J., Emmons, L. K., Al-Saadi, J. A., Orlando, J. J., & Soja, A. J. (2011). The Fire INventory from NCAR (FINN): A high resolution global model to estimate the emissions from open burning. *Geoscientific Model Development*, *4*(3), 625–641. https://doi.org/10.5194/gmd-4-625-2011

Wolfe, G. M., Nicely, J. M., St Clair, J. M., Hanisco, T. F., Liao, J., Oman, L. D., et al. (2019). Mapping hydroxyl variability throughout the global remote troposphere via synthesis of airborne and satellite formaldehyde observations. *Proceedings of the National Academy of Sciences of the United States of America*, *116*(23), 11171–11180. https://doi.org/10.1073/pnas.1821661116

Woo, J.-H., Choi, K.-C., Kim, H. K., Baek, B. H., Jang, M., Eum, J.-H., et al. (2012). Development of an anthropogenic emissions processing system for Asia using SMOKE. *Atmospheric Environment*, *58*, 5–13. https://doi.org/10.1016/j.atmosenv.2011.10.042

Yu, K., Jacob, D. J., Fisher, J. A., Kim, P. S., Marais, E. A., Miller, C. C., et al. (2016). Sensitivity to grid resolution in the ability of a chemical transport model to simulate observed oxidant chemistry under high-isoprene conditions. *Atmospheric Chemistry and Physics*, *16*(7), 4369–4378. https://doi.org/10.5194/acp-16-4369-2016

Zakoura, M., & Pandis, S. N. (2018). Overprediction of aerosol nitrate by chemical transport models: The role of grid resolution. *Atmospheric Environment*, *187*, 390–400. https://doi.org/10.1016/j.atmosenv.2018.05.066

Zhang, G. J., & McFarlane, N. A. (1995). Sensitivity of climate simulations to the parameterization of cumulus convection in the Canadian climate centre general circulation model. *Atmosphere-Ocean*, *33*(3), 407–446. https://doi.org/10.1080/07055900.1995.9649539

Zhao, Y., Saunois, M., Bousquet, P., Lin, X., Berchet, A., Hegglin, M. I., et al. (2019). Inter-model comparison of global hydroxyl radical (OH) distributions and their impact on atmospheric methane over the 2000–2016 period. *Atmospheric Chemistry and Physics*, *19*(21), 13701–13723. https://doi.org/10.5194/acp-19-13701-2019